Department of Physics and Astronomy

University of Heidelberg

Master Thesis

in Physics

submitted by

Michele Piero Blago

born in Heidelberg

2017

Characterisation of the Photon Detection System for the LHCb RICH Detector Upgrade

This Master Thesis has been carried out by Michele Piero Blago

at the

Physikalisches Institut Heidelberg

under the supervision of

Prof. Dr. Ulrich Uwer

and the external supervision of

Dr. Carmelo D'Ambrosio

Dr. Sajan Easo

Abstract

The LHCb Experiment will be upgraded during Long Shutdown II of the Large Hadron Collider (LHC) in 2019 and 2020. The goal of the upgrade is to efficiently use the increased instantaneous luminosity in LHC Run 3 and to collect data at the proton collision rate of 40 MHz. The Ring Imaging Cherenkov (RICH) particle identification detectors will be upgraded to perform in the new operating conditions with continuing reliability. The photon detection system will be replaced using multi-anode photomultiplier tubes (MaPMTs) and associated read-out electronics.
The photon detection chain was studied at CERN using a pulsed laser to test the system under high event rates and high photon intensities. The behaviour of two types of MaPMTs which are foreseen for the upgrade is presented for varying rates and intensities, and different applied bias voltages.
A simulation was created to model the photon detection chain using the Geant4 simulation toolkit. The RICH Upgrade test beam using 180 GeV positive hadrons from CERN SPS in October 2016 was recreated in the simulation. Data from simulation and test beam are analysed and compared as a consistency check. Comparing the number of detected photo-electrons in simulation and data allows the photon detection efficiency to be determined.

Zusammenfassung

Am LHCb Experiment wird während des Long Shutdown II des Large Hadron Colliders (LHC) in den Jahren 2019 und 2020 ein Upgrade durchgeführt. Ziel dieses Upgrades ist, die erhöhte Luminosität des LHC Run 3 effizient zu nutzen und Daten mit der Protonen Kollisionsrate von 40 MHz zu sammeln. Die Ring Imaging Cherenkov (RICH) Detektoren stellen einen wesentlichen Bestandteil der Teilchenidentifikation von LHCb dar. Die Detektoren erhalten ein Upgrade, um unter den erschwerten Bedingungen in Run 3 weiterhin verlässliche Ergebnisse zu liefern. Das gesamte Photodetektionssystem wird ersetzt, mit Multi-Anode Photomultiplier Tubes (MaPMTs) als neue Photodetektoren in Kombination mit der entsprechenden Ausleseelektronik.
Das Photodetektionssystem wurde am CERN in Labortests unter hohen Photon Ereignisraten und Okkupanzen mithilfe eines Pulslasers untersucht. Das Verhalten der zwei für das Upgrade vorgesehenen MaPMT-Arten wird erläutert, in Abhängigkeit von Ereignisrate und Intensität und für verschiedene Ruhespannungen.
Eine Computersimulation des Photodetektionssystems wurde unter Verwendung des Geant4 Toolkits nach Modell des RICH Upgrade Teststrahl Experiments von Oktober 2016 erstellt, in welchem der sekundäre 180 GeV Teilchenstrahl des CERN SPS aus positiven Hadronen verwendet wurde. Die Daten aus Simulation und Teststrahl Experiment wurden analysiert und verglichen, um deren Übereinstimmung zu untersuchen. Der Vergleich der Anzahl an detektierten Photoelektronen in Simulation und Daten ermöglicht die Bestimmung der Photonendetektionseffizienz.

Contents

1 Introduction

The LHCb Experiment is one of the four major experiments at the Large Hadron Collider (LHC) at CERN (European Organisation for Nuclear Research). The energy scale in combination with the instantaneous luminosity of particle interactions at the LHC is unprecedented, which allows for fundamental tests of the Standard Model of Particle Physics. LHCb is designed for high sensitivity searches of charge parity (CP) violations in beauty hadron decays and further high precision studies of the heavy flavour sector. To significantly decrease statistical uncertainties and enhance the precision of the measurements, LHCb will be upgraded during the Long Shutdown II of the LHC in 2019-2020, to collect data with five times higher instantaneous luminosity and at a proton collision rate of 40 MHz.

This thesis is focused on the characterisation and simulation of a photon detection system and its read-out electronics, for a Ring Imaging Cherenkov (RICH) detector upgrade. The RICH detector system is responsible for particle identification within the LHCb (Large Hadron Collider beauty) experiment. LHCb and the LHCb Upgrade will be laid out in context with the motivation for the upgrade of the RICH detectors. The RICH Upgrade photon detection system is tested at high incident photon rates and occupancies. A simulation is built to model the detection efficiency of the system and compared to data from a dedicated test beam experiment.

Chapter 2 gives a brief introduction to the LHC and an overview of the LHCb Experiment and its sub-detectors. The upgrade of the LHCb and the resulting modifications of the detector systems are illustrated.

Chapter 3 focuses on the RICH detectors and its current photon detection system. The technical challenges of the current system facing the demands of the upgraded LHCb environment are explained. This motivates the upgrade of the RICH photon detection system and read-out electronics. The components of the RICH Upgrade system are depicted.

Chapter 4 describes laboratory tests of the photon detection system and its electronics under conditions close to the RICH Upgrade environment in terms of photon rate and occupancy. The results show stable performance for nominal powering conditions. Lowered supply voltage powering would increase the lifetime of the system but indicates detection inefficiencies at high rates and high occupancies. Preliminary tests of a modified powering scheme are conducted to motivate further studies.

Chapter 5 illustrates a simulation, designed for this study to model the RICH Upgrade photon detection system. The simulated set-up is constructed to represent the latest RICH Upgrade test beam experiment. Data from both simulation and test beam are analysed and compared with the goal to probe the Collaboration's understanding of the efficiencies and technical functioning of the photon detectors foreseen for the upgrade.
The results of the studies are brought together and summarised in the conclusion in Chapter 6.

2 The Large Hadron Collider and the LHCb Experiment

The Large Hadron Collider (LHC) at CERN and its four major experiments ATLAS, ALICE, CMS, and LHCb serve the purpose to study the Standard Model of Particle Physics. This section gives a brief introduction to the LHC and its experiments, with focus on the LHCb experiment and its sub-detectors.

2.1 The LHC Machine

The LHC is the world's largest and most powerful synchrotron particle-particle accelerator of protons or heavy ions. It was constructed in the 26.7 km long circular tunnel of its predecessor, the Large Electron Positron collider (LEP) [1]. It is located about 100 m underneath the border between France and Switzerland in the Geneva area. The LHC features two counter rotating beams, separated in two beam pipes. The beam pipes cross at four positions, marking the interaction points and the location of the four major LHC experiments. Figure 2.1 shows a schematic overview of the accelerator complex at CERN. The protons are produced from ionised hydrogen. Before injection into the LHC machine, they are accelerated in several stages. First, the protons reach an energy of 50 MeV in the LINAC2 linear accelerator, the Proton Synchrotron Booster accelerates the particles to 1.4 GeV. Afterwards, they are injected into the Proton Synchrotron to reach 25 GeV, and then the Super Proton Synchrotron, where they are accelerated to 450 GeV. Heavy ions are produced from a different source and accelerated in LINAC3, followed by the Low Energy Ion Ring. Afterwards, the acceleration stages are similar, but with different energies.
During Run 1 of the LHC, particles collided with a centre-of-mass energy of 7 GeV in 2011 and 8 GeV in 2012, separated by 50 ns each. In 2015, with the start of LHC Run 2, the centre-of-mass collision energy increased to 13 TeV.
The LHC consists of eight straight acceleration segments and eight arcs in which the beams are bent by superconducting twin-bore magnets. A dipole field strength of

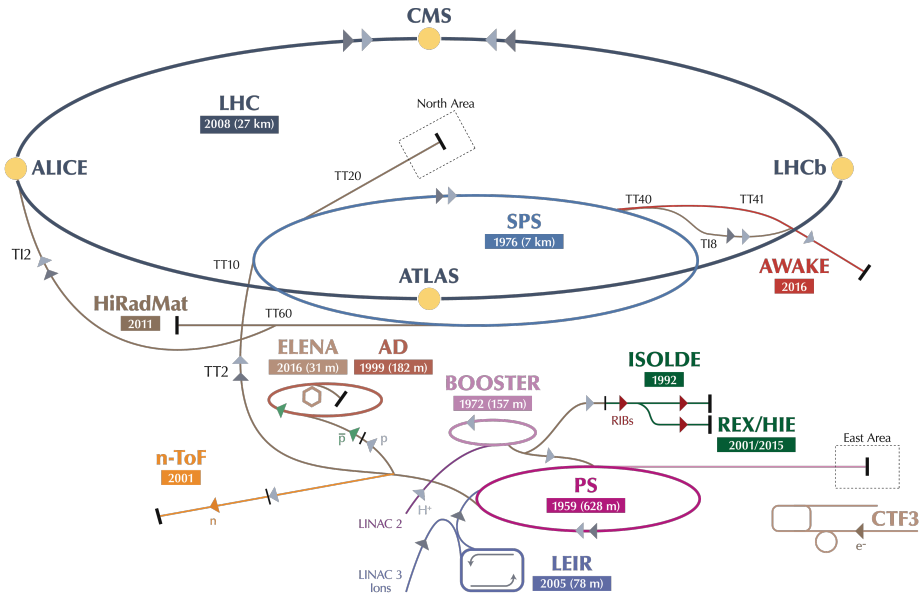

Figure 2.1: Schematic of accelerator complex at CERN. The acceleration chain is shown, the four main collision points are marked by a yellow dot [2].

8.33 T of the magnets is required to reach the nominal peak beam energy of 7 TeV, corresponding to a centre-of-mass energy of 14 TeV. In nominal running conditions, the LHC has a design instantaneous luminosity of 10^{34} cm^{-2}s^{-1}, containing 2808 bunches with 1.15×10^{11} protons each. The bunches are colliding at a design value of every 25 ns, corresponding to a rate of 40 MHz. The LHC is also capable to accelerate heavy ions (Pb-Pb) to 2.76 TeV, colliding with a centre-of-mass energy of 1.5 PeV and 10^{27} cm^{-2}s^{-1} instantaneous luminosity. The LHC is described in full detail in [1].

At the end of the 2016 run of the LHC, the design instantaneous luminosity was exceeded by 40 %, reaching 1.4×10^{34} cm^{-2}s^{-1} [3]. The nominal centre-of-mass collision energy of 14 TeV at 40 MHz collision rate is expected to be reached after Long Shutdown II of the LHC in 2021.

Particles collide simultaneously at the four interaction points, where the four experiments are located. ATLAS and CMS are general purpose detectors, designed for good geometric coverage and calorimetry to reconstruct missing energy in the events. The physics programme of the the two detectors is broad, with a focus on Higgs and physics beyond the Standard Model. The ALICE experiment has the objective to study ion-ion collisions and in particular the Quark Gluon Plasma. The LHCb experiment will be explained in more detail in Section 2.2.

2.2 The LHCb Experiment

The Large Hadron Collider Beauty experiment is dedicated to studying CP-violations and rare decays of hadrons containing a beauty or charm quark [4]. In particular, the experiment studies the components of the CKM matrix of the Standard Model and searches for indications of physics beyond the Standard Model. Beauty or charmed hadrons are mostly generated by gluon-gluon interactions. The gluons in this type of interaction often carry a largely differing fraction of the beam particle momentum, causing a boost of the resulting particles along the beam line. LHCb is designed as a single-arm forward spectrometer to make use of this effect. Figure 2.2 shows a schematic side view of LHCb and its sub-detectors. The particle interaction point is located at the origin of the coordinate system. It has full tracking coverage in

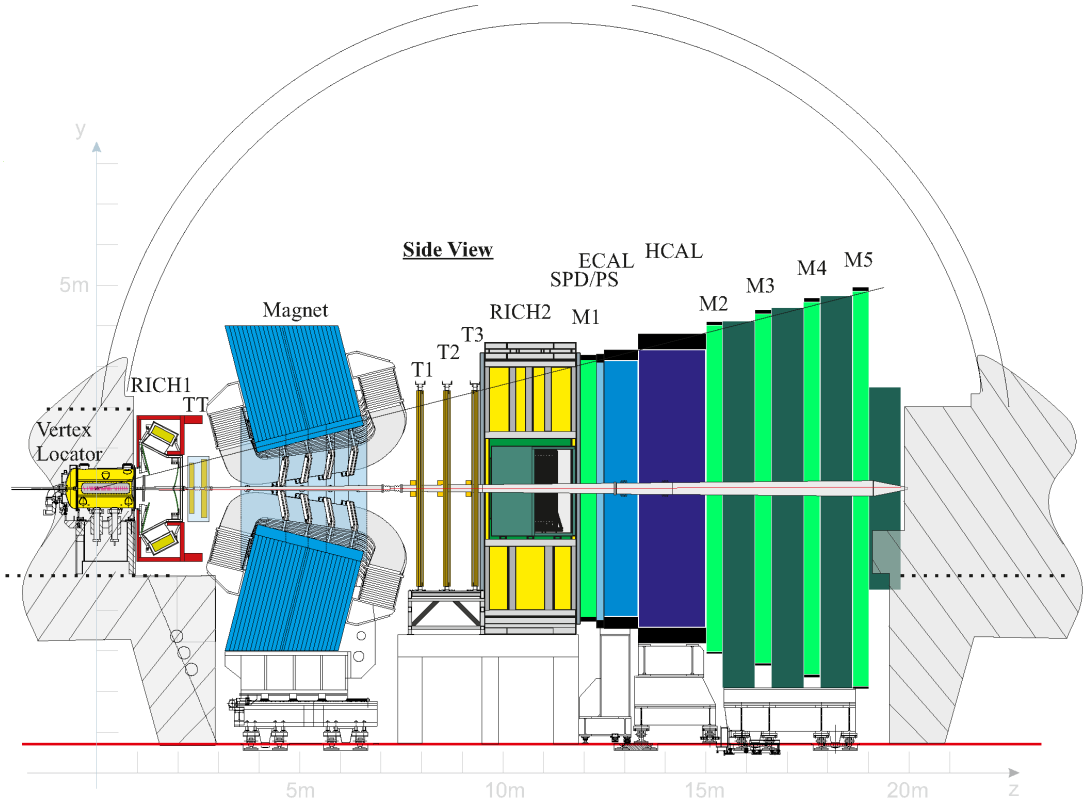

Figure 2.2: Schematic side view of the LHCb experiment and its sub-detectors [4].

the pseudorapidity range $1.8 < \eta < 4.9$, which allows studying boosted hadrons of interest. Figure 2.3 shows the produced number of $b\bar{b}$ pairs as a function of polar angle (Figure 2.3a) and pseudorapidity (Figure 2.3b). The LHCb acceptance is

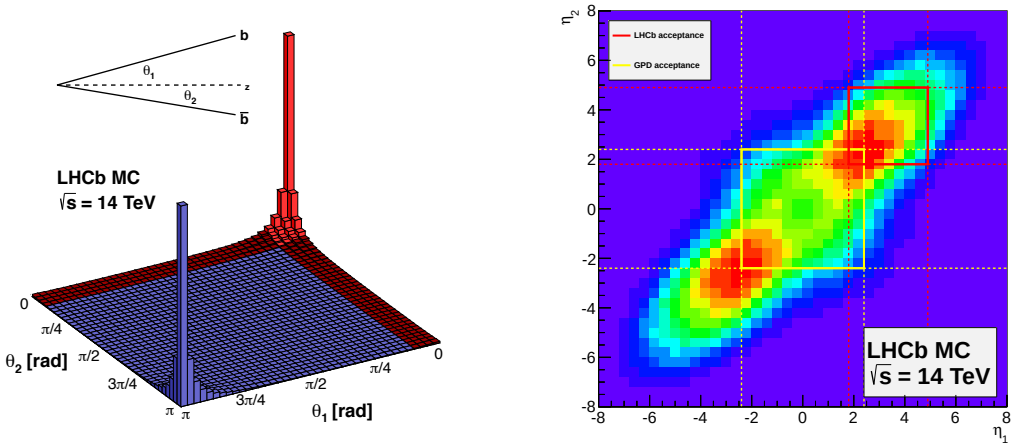

(a) (b)

Figure 2.3: $b\bar{b}$ production angle plots [5]. Produced number of $b\bar{b}$ pairs as a function of polar angle θ (a) and pseudorapidity (b). LHCb acceptance is marked in red, pseudorapidity acceptance for the general purpose detectors in yellow.

marked in red.

The design instantaneous luminosity of the LHCb experiment is 4×10^{32} cm^{-2}s^{-1}, which is by a factor 50 less than the nominal value for ATLAS and CMS. It is reduced by defocusing the beam locally before reaching the LHCb interaction point. This design luminosity accounts for the high precision demands of the LHCb physics, regarding the reconstruction of decay chains, by lowering the number of p-p collisions per bunch crossing and hence maintaining a low pile-up.

The individual components of the LHCb detector are explained in more detail in the following.

2.2.1 Magnet

A warm [1] dipole magnet [6] with an integrated magnetic field of 4 Tm bends charged particles to allow measuring their momentum in the ±300 mrad horizontal and ±250 mrad vertical forward acceptance. To minimise systematic uncertainties due to detector asymmetries, the polarisation of the magnet is changed frequently during data taking.

[1] Referring to the fact that the magnet does not require cryogenic cooling.

2.2.2 Particle Tracking

To reliably determine particle momentum, impact parameter, and to achieve good primary vertex resolution, a combination of three tracking systems is used in LHCb: the Vertex Locator (VELO) at the interaction point, the Tracker Turicensis (TT) in front of the magnet, and the Tracking stations located behind the magnet, split in Inner and Outer Tracker (IT & OT). The deflection of the charged particles passing through the field of the magnet allows measuring their momentum.

Vertex Locator

The Vertex Locator is a silicon micro-strip detector, providing track measurements close to the interaction point (IP) [7, 8]. This allows reconstructing the primary interaction vertex, as well as secondary vertices as from the decay of c- and b-hadrons, which is essential for the LHCb physics programme. VELO comprises 42 micro-strips with radial and azimuthal geometry and a pitch of 38 to 120 μm. During stable beam conditions, the inner parts of the modules have a distance of 7 mm to the beam axis. VELO consists of two halves, which are retracted during filling of the LHC or in case the *Beam Conditions Monitor* of LHCb registers abnormal beam conditions. A schematic of the VELO is shown in Figure 2.4.

Tracker Turicensis (TT)

The Tracker Turicensis (TT)[2] [9] is one of the two silicon tracker stations of LHCb. The modules are arranged in a x-u-v-x geometry, meaning that the strips in the first and last layer are oriented vertically, along the y-axis, and the middle two layers are tilted by $\pm 5°$, respectively. The tilting angle with respect to the vertical allows stereo measurements. TT covers the entire acceptance of LHCb, apart from the beam pipe region, and is located upstream of the magnet. The schematic layout of the sub-detector is shown in Figure 2.5a.

[2]Previously named Trigger Tracker. Changed to Tracker Turicensis (Turicensis: lat. *Zürich*). Universität Zürich was the main contributor to TT.

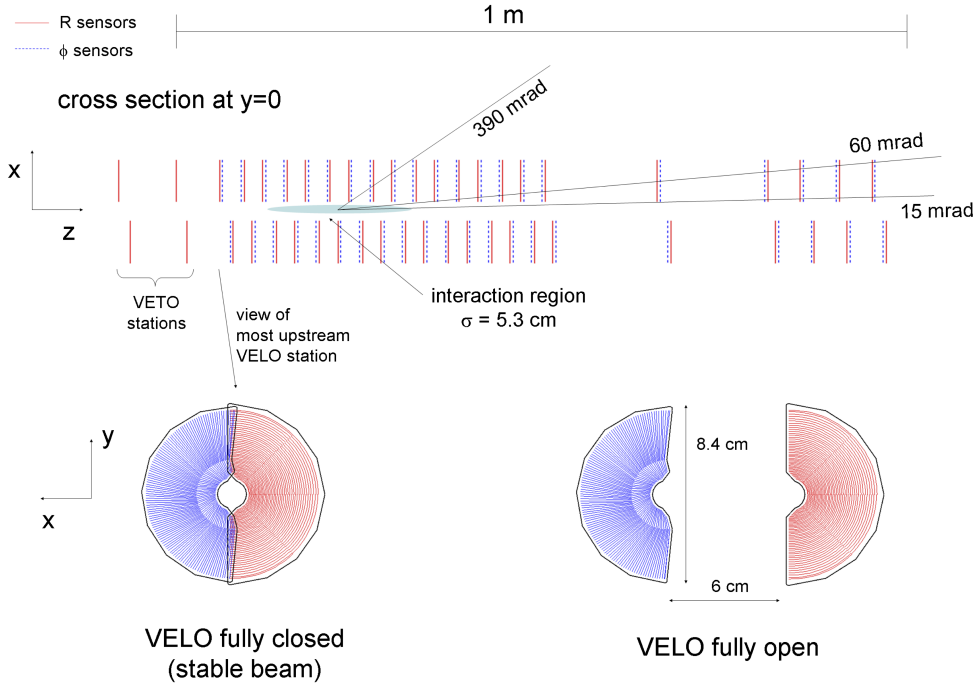

Figure 2.4: Schematic of Vertex Locator (VELO). Distribution of modules along the z-axis (top) and VELO in open and closed position (bottom) [7].

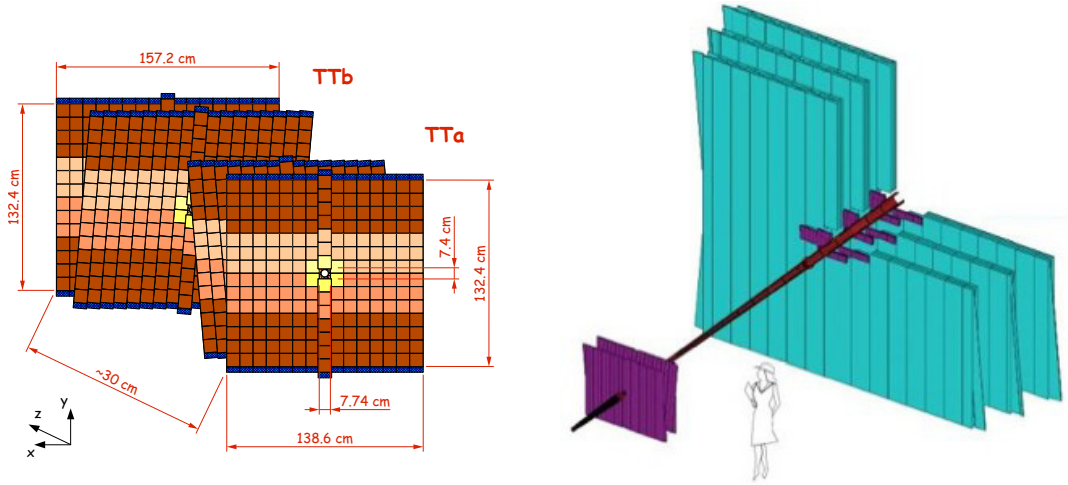

(a) (b)

Figure 2.5: Schematic of Tracker Turicensis (TT) modules (left) [10]. Tracking system with silicon tracker planes in purple and OT planes in blue (right) [11].

Inner Tracker and Outer Tracker

The Inner Tracker (IT) is the second silicon tracker station. It is located on the downstream side of the magnet and cross-shaped, covering the area close to the beam pipe with a high track density [12]. The Outer Tracker (OT) [11, 13] is a drift-tube detector made of straw-tube arrays, covering the area outside the IT region, with a lower track density. The straw-tube arrays have a diameter of 4.9 mm, filled with a mixture of Argon (70 %), CO_2 (28.5 %), and O_2 (1.5 %), providing a drift time below 50 ns and coordinate resolution of about 200 μm. The tube arrays are arranged in 200 modules. A schematic of the silicon tracker system and the OT is shown in Figure 2.5b.

2.2.3 Particle Identification

To perform b quark flavour tagging and to distinguish signal event signatures from background, particle identification (PID) is a key for LHCb physics. The information of several PID stations is combined to achieve this goal. Two RICH detectors are responsible for discriminating between charged hadrons. Muon chambers at the downstream end of the detector identify muon tracks. The calorimetry system distinguishes between electrons, photons, and hadrons. From the combined information a particle hypothesis likelihood is derived.

The RICH System

The two Ring Imaging Cherenkov (RICH) detectors have the primary purpose of distinguishing charged hadrons (π, K, p) [9, 14]. The RICH detectors exploit the Cherenkov effect, i.e. the fact that particles travelling through a medium with a velocity greater than the velocity of light in the same medium, emit photons under a characteristic angle (θ_{Ckv}) with respect to the particle track. A system of tilted flat and spherical mirrors is used to focus the resulting light cone into a ring, and to project it onto the photo-detection system, consisting of Hybrid Photon Detectors (HPDs). The radius of the cone is used to reconstruct the Cherenkov angle θ_{Ckv}, and consequently the particle velocity. The tracking system provides momentum information for the particle candidates. Different particle hypotheses are are used to predict corresponding Cherenkov cones. These are compared with the photon distributions of the RICH detectors, allowing to determine the particle type. A

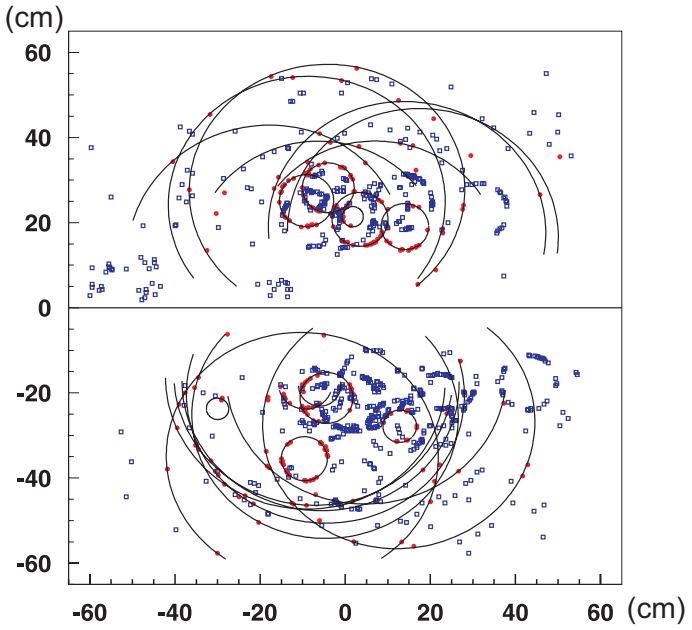

Figure 2.6: RICH1 event display with ring fits to photon hits [9].

typical event display of RICH 1 is shown in Figure 2.6.
Dividing the RICH system into two separated detectors accounts for the distinct inverse dependence between momentum and polar angle. The upstream detector, RICH1, located between VELO and TT, covers the entire angular acceptance in the range $15-300\,\text{mrad}$ and the momentum range $2-40\,\text{GeV/c}$. RICH2, which is positioned downstream of the magnet, behind the tracking stations, covers $15-120\,\text{mrad}$ and $15-100\,\text{GeV/c}$. C_4F_{10} gas (refractive index $n = 1.0014$) is used in RICH1 as a Cherenkov medium, and CF_4 ($n = 1.0005$) in RICH2. During LHC Run 1 silica aerogel ($n = 1.03$) was used in RICH1 in addition to the gas, but was removed during the Long Shutdown I between 2013 and 2015.
The different refractive indices of the Cherenkov radiators allow for particle identification in certain momentum ranges. This working principle and the RICH system is described in more detail in Section 3.3.

Calorimeters

The calorimetry system [15] consists of two main bodies, the electromagnetic (ECAL) and the hadronic (HCAL) calorimeter. On the upstream side of the ECAL a Scintillating Pad Detector (SPD), and a Preshower Detector (PD) is added to the calorimetry system. The objective of the system is to distinguish between electrons and

photons, and hadrons, as well as to measure their position and energy. In addition, the measured transverse energy is passed to the first level trigger (L0) and is used to trigger on electrons, photons, and hadrons. When particles traverse the ECAL stations, particle showers are created by pair production. For both calorimeters scintillation light is produced in the scintillation material of the detectors and guided through wavelength shifting fibres to photomultiplier tubes for detection. The ECAL is a sampling calorimeter with shashlik structure, comprised of lead with up to 25 radiation lengths interchanging with scintillator material, providing an energy resolution of $\sigma_E/E = \frac{10\%}{\sqrt{E/GeV}} + 1\%$. The HCAL sampling calorimeter consists of iron layers of a total thickness up to 5.6 interaction lengths, alternating with scintillator layers also in a shashlik structure, providing a resolution of $\sigma_E/E = \frac{70\%}{\sqrt{E/GeV}} + 10\%$. The varying first term of the calorimeter resolutions is due to statistical fluctuations in the shower creation, the constant second term has a systematic origin.

Muon system

The muon system [16–18] consists of five Multiwire Proportional Chamber (MWPC) layers. The first one is located upstream the calorimeters, featuring a Gas Electron Multiplier (GEM), which is more radiation resistant than the MWPC, in the high-flux region near the beam pipe. The other four muon detection layers are located on the downstream side of the calorimeters, as the outermost part of the LHCb detector. These layers are interchanging with iron absorbers of 80 cm thickness, summing up to 20 hadronic interaction lengths in combination with the HCAL. The muon system provides essential information to the L0 and the *High Level Trigger* (HLT), since muons occur in many final states of CP-sensitive decays, such as $B_S^0 \to J/\psi\phi$, or rare decays as $B_S^0 \to \mu^+\mu^-$. Muons are identified with 95 % efficiency, other particles are misidentified as muons in about 2 % of cases [18].

Combining the information of the RICH detectors, the calorimeters, and the muon system allows to define a particle hypothesis (π, K, μ, p). Since charged pions are the most common particles within the LHCb system, the likelihood that a given particle fulfills the hypothesis of being a certain particle X is divided by the likelihood that the particle is a charged pion. To account for the wide probability distribution, the logarithm is taken. The resulting Delta Log Likelihood (DLL) is the typical variable

used for PID selection:

$$\mathrm{DLL}_{X\pi} = \log \mathcal{L}_X - log\mathcal{L}_\pi. \tag{2.1}$$

2.2.4 Trigger

The trigger system [19, 20] selects events of a given signature and reduces the amount of uninteresting data. Beauty and charmed hadron decays have characteristically large lifetimes and large invariant masses. The long lifetimes are responsible for a large impact parameter relative to the primary vertex. The large masses result in a high transverse momentum of the daughter particles of the hadron decay.
To select signature events, a multi level trigger system is used, consisting of the L0 hardware trigger, and the High Level Trigger (HLT) implemented in software.

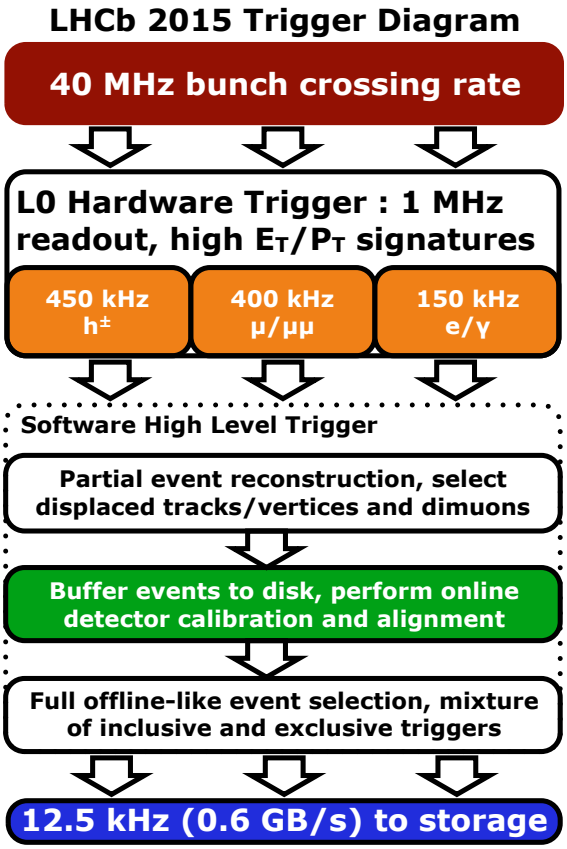

Figure 2.7: LHCb trigger scheme for LHC Run 2 [21].

Level-0 Trigger

The Level-0 hardware trigger is operating synchronous to the 40 MHz bunch crossing clock of the LHC. In the calorimeters mainly events with high transverse energy E_T are selected. The muon chambers select single- or di-muon events with high transverse momentum p_T. If one of these criteria is above the respective threshold, the event is further processed. This reduces the rate to 1 MHz, with a latency of $4\,\mu$s.

The High Level Trigger

The HLT software trigger is performing a reduced version of the offline event reconstruction on the events selected by the L0-trigger. This analysis is performed by the Event Filter Farm (EFF) in two stages, HLT1 and HLT2. After the L0 trigger and partial reconstruction, selected events are stored to the buffer for online calibration and alignment of the detector. Offline-like reconstruction, PID information from the RICH system, and inclusive and exclusive selections result in a final trigger decision.

2.3 The LHCb Upgrade

To improve the statistical significance of the most of LHCb's measurements, the experiment will undergo a substantial upgrade during the Long Shutdown II of the LHC in 2019-2020. The goal is to operate at an instantaneous luminosity of 2×10^{33} cm^{-2}s^{-1} [22, 23]. The higher luminosity allows increasing the data sample significantly. Over the course of 10 years of operation LHCb aims to collect 50 fb^{-1} of data.

The limiting factor to fully exploit the higher luminosity is the L0 hardware trigger. The existing front-end electronics is limited to 1 MHz readout which requires a strong selection of the first level trigger, forming decisions based on characteristic features, such as transverse momentum, as described in Section 2.2.4. An increase in luminosity requires higher thresholds on the event signatures. This affects especially purely hadronic decays, cutting a large part of the signal events.

The LHCb detector upgrade avoids this limitation by removing the L0 hardware trigger and by reading the detector information at 40 MHz. Events are recorded and sent to the LHCb data acquisition farm at the full event rate of the LHC and processed by a software trigger (Figure 2.8a). The software trigger features a sim-

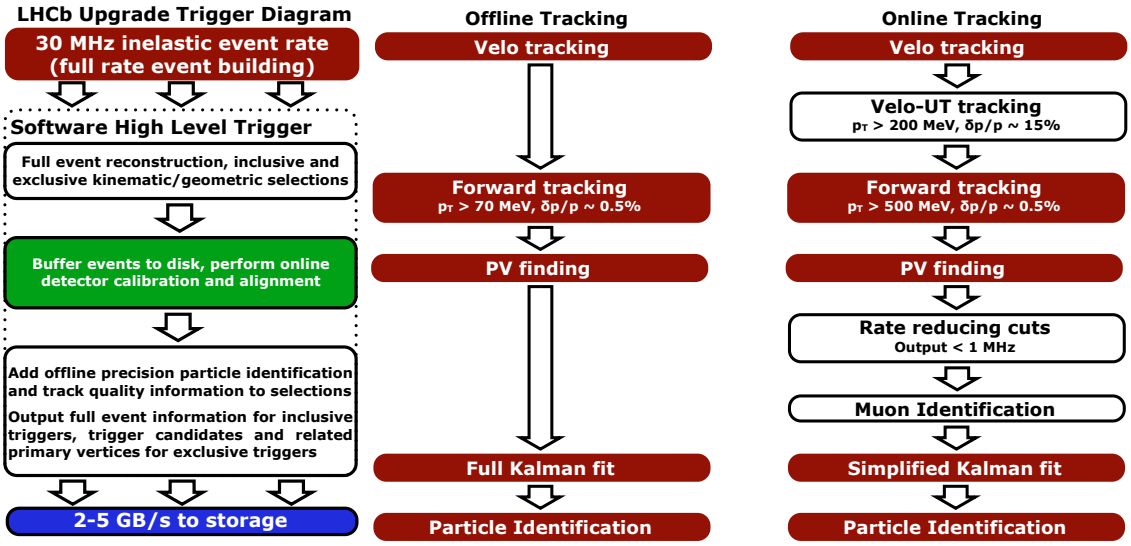

(a) (b)

Figure 2.8: Trigger flow of the upgraded LHCb experiment, fully implemented in software (a). Offline and online reconstruction sequence (b). The software trigger includes a reduced version of the offline reconstruction [24].

plified version of the offline reconstruction to increase its efficiency.

The upgrade imposes two major challenges to the sub-detectors of LHCb. Their front-end electronics has to be able to read out at 40 MHz due to the trigger-less read-out and the detectors have to withstand a five times higher luminosity in comparison to Run 2. The upgraded LHCb features a new Vertex Locator (VeLoPix), the Upstream Tracker (UT), the Scintillating Fibre Tracker (SciFi), changes to the calorimetry system and muon system, and a major upgrade of the RICH detectors. A schematic side view of the upgraded LHCb experiment is shown in Figure 2.9.

2.3.1 Tracking Upgrade

VeLoPix will be able to operate at the 40 MHz and will replace the current Vertex Locator, featuring pixels of size $55 \times 55\,\mu m^2$ and a lower material budget [26]. It consists of two halves and the minimal distance of the 26 modules to the interaction point will be 5.1 mm. These changes yield a better resolution and improved track reconstruction. Figure 2.11 shows a schematic of one VeLoPix half and the sensors in the closed position.

The TT will be replaced by the Upstream Tracker (UT). The four new silicon

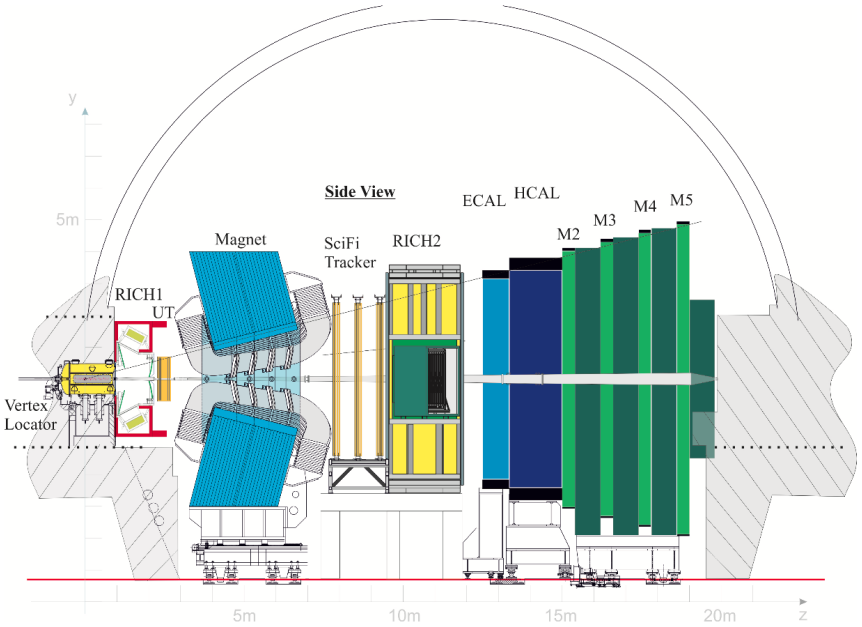

Figure 2.9: Schematic side view of upgraded LHCb detector, featuring VeLoPix, UT, SciFi, and upgraded RICH detectors and calorimetry [25].

strip planes maintain the x-u-v-x geometry. The planes cover a larger part of the LHCb acceptance. Their micro-strip sensors are read out at 40 MHz by Application Specific Integrated Circuits (ASICs), which are directly connected to the sensors.

The tracking systems on the downstream side of the magnet will be replaced by a single Scintillation Fibre (SciFi) tracker [28]. It consists of three stations of four layers each, maintaining the x-u-v-x geometry and $\pm 5°$ tilt of the two middle layers with respect to the vertical. Each detections layer should not exceed a material budget of 1 % X_0. The scintillating fibres will have a nominal diameter of 250 μm and guide the photons to multichannel silicon photomultipliers (SiPMs). The SiPMs are read out by custom designed ASICs with 25 ns signal integration length and cooled to $-40\,°$C to reduce thermal noise. The front-end electronics operate with a 40 MHz trigger-less read-out.

2.3.2 PID Upgrade

The current Hybrid Photon Detectors (HPDs) of the RICH detectors have the 1 MHz read-out electronics integrated inside the vacuum tube. To operate at 40 MHz the HPDs will be replaced by multi-anode photomultiplier tubes and external read-out

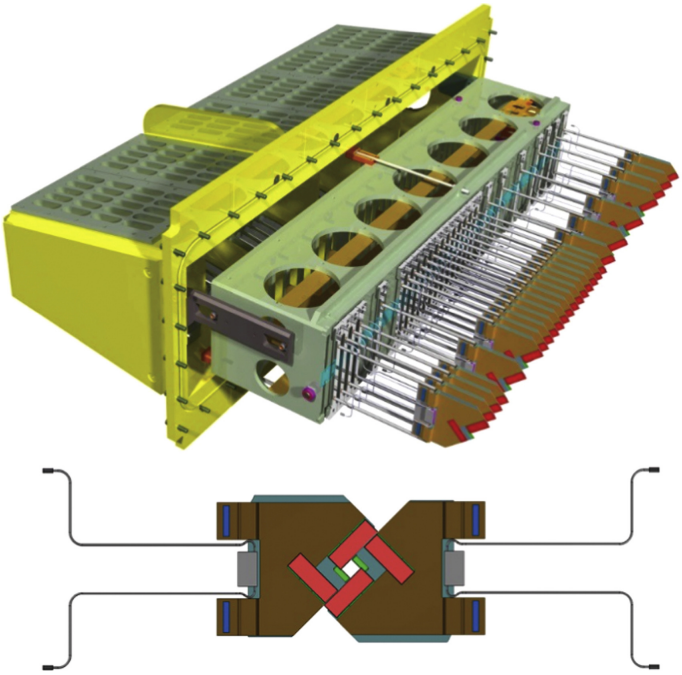

Figure 2.10: Schematic of VeLoPix detector half with 26 pixel modules (top) and sensors in the closed configuration (bottom) [27].

electronics. The mirror design of the detectors will be changed to account for higher occupancies. The RICH system and its upgrade are explained in detail in Section 3.4.

The electronics of the calorimeter system will be adapted to the read-out rate. With the removal of the L0, the PS and SPD will loose their main purpose and will be removed.

The first station of the muon system will be removed due to the occupancy increase. Since the software trigger relies on information from the muon system, the back-end electronics will be modified to provide the required information.

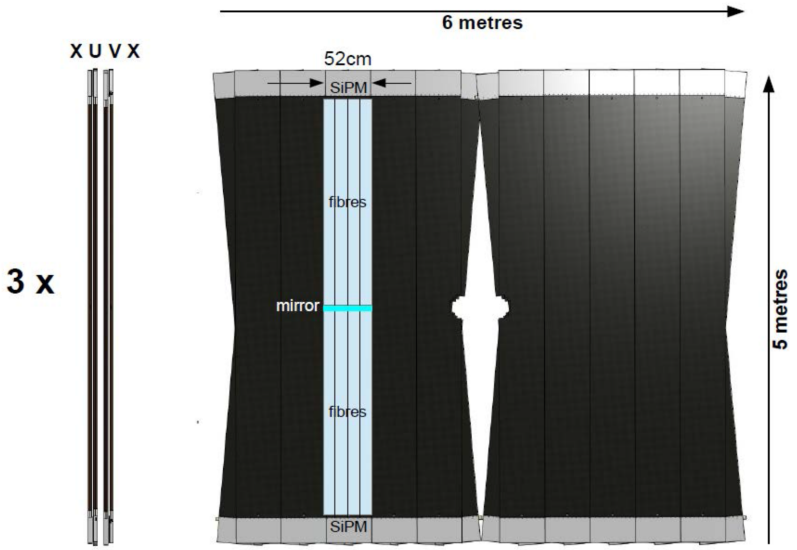

Figure 2.11: Schematic of one SciFi detector station. A module is highlighted, containing 2×4 fibre mats. Light is mirrored on one side of the fibre end and by SiPMs on the outer part of the detector [28].

3 The LHCb RICH System: Status and Upgrade

The LHCb Ring Imaging Cherenkov (RICH) detectors are responsible for particle identification (PID) of charged hadrons. The detectors exploit the Cherenkov effect to distinguish between π, K, and p. The RICH system consists of two detectors, one located upstream of the magnet, close to the Vertex Locator, and the second one downstream of the tracking stations. During the Long Shutdown II of the LHC, the photon detection system and read-out electronics of the RICH detectors will be replaced to operate at the collision rate of 40 MHz.
This chapter provides an introduction to the theoretical background of Cherenkov radiation and gives a brief overview of Cherenkov detection systems. The current LHCb RICH photon detectors are illustrated to motivate the upgrade, and the working principle of the RICH Upgrade photon detectors is explained.

3.1 Cherenkov effect

The operation principle of Cherenkov detection systems is based on the effect that charged particles emit photons when they traverse a medium with a velocity v_p greater than the velocity of light in the medium c_m:

$$v_p > c_m = \frac{c}{n(\omega)}, \tag{3.1}$$

where c is the speed of light in vacuum and $n(\omega)$ the refractive index of the medium, which depends on the frequency ω of the emitted photons. This effect was first observed by P. A. Cherenkov in 1934 [29, 30] and theoretically formulated by I. Frank and I. Tamm in 1937 [31]. Cherenkov, Frank, and Tamm were collectively awarded the Nobel prize in 1958.
The light is emitted at a constant angle θ_{Ckv} relative to the direction of propagation

of the charged particle, for a refractive index $n(\omega)$:

$$\cos\theta_{Ckv} = \frac{1}{n(\omega)\beta}, \tag{3.2}$$

where $\beta = v_p/c$ is the ratio between the velocity of the particle v_p and vacuum speed of light c. Cherenkov radiation is caused by the constructive interference of electromagnetic waves from the atoms which are polarised by the traversing charged particle if it fulfills Equation 3.1. While the Cherenkov angle θ_{Ckv} is constant for a fixed refractive index, the azimuthal emission angle is random. This results in the creation of a light cone relative to the flight direction of the particle.
From Equation 3.2 follows a Cherenkov radiation condition for β, due to $|\cos\theta| \geq 1$. Below $\beta_{thr} = 1/n$ the Chernkov effect does not occur. β_{thr} is known as Cherenkov threshold.
For high energies of the particle, β approaches unity: $\beta \to 1$. This means that a maximal Cherenkov angle θ_{Ckv}^{max} exists:

$$\cos\theta_{Ckv}^{max} = \frac{1}{n}. \tag{3.3}$$

Following this equation, particles become indistinguishable at large momenta, since for different masses the Cherenkov angle change is marginal. The angle θ_{Ckv}^{max} is called saturation angle. The angle at which momentum saturation occurs is dependent on both the refractive index of the medium and the mass of the particle. As a consequence, the effective momentum range for a Cherenkov detector is limited in the direction of low momenta by the Cherenkov threshold β_{thr}, and for high momenta by the saturation effect.
The specific light yield of a particle passing through a medium is given by the Frank-Tamm equation:

$$\frac{d^2N}{dEdx} = \frac{\alpha}{\hbar c} Z^2 \left(1 - \frac{1}{n^2\beta^2}\right), \tag{3.4}$$

where dN is the number of photons generated over a length dx and with an energy dE, for a particle of charge Z. α represents the fine structure constant, $\hbar$ is the reduced Planck constant, and c the vacuum light speed. For most practical purposes the particle charge Z is ± 1 in units of e, the elementary charge. For a straight

particle track, integration yields

$$\frac{dN}{dE} = 370L\left(1 - \frac{1}{n^2\beta^2}\right)[\text{GeV} \cdot \text{cm}]^{-1}, \tag{3.5}$$

after inserting the constants. The number of emitted photons can now be determined for a radiator of length L in cm, when integrating over the energy range dE (in GeV), if β of the incoming particle and the refractive index are known. To make an estimation about the number of detected photons, additional parameters have to be taken into account, such as quantum efficiency, and geometric acceptance of the photon detectors.
The emission of Cherenkov photons is possible in gaseous, liquid, and solid media. To calculate the photon propagation speed in dispersive media, it is important to separate *phase* refractive index n_p and *group* refractive index n_g. When considering the refractive index of a medium, as in the previous context, the phase refractive index is referred to. The photon speed in that medium is determined by the group refractive index, which is related to the phase refractive index by the change of n_p with energy E:

$$n_g = n_p + E\frac{dn_p}{dE}. \tag{3.6}$$

As shown in Equation 3.2, the velocity β of a particle can be determined when the Cherenkov angle is measured and the phase refractive index of the medium is known including the effect of chromatic dispersion. In combination with the momentum information from a tracking system, the mass m of the particle can be determined. This is achieved by using the relation

$$p = \gamma m \beta c, \tag{3.7}$$

where γ is the Lorentz factor. The mass m hypothesis together with the charge information from the track curvature, identify the particle.

3.2 Cherenkov detectors

Using the Cherenkov effect to identify particles was made possible through the development of photomultiplier tubes, which allow the detection of small quantities of light. The first concept for a RICH design was proposed in 1977 by T. Ypsilantis

and J. Seguinot [32]. This led to the first RICH detector, installed in the E605 experiment at Fermi National Accelerator Laboratory (FNAL).

The momentum detection range of a RICH detector is set by the product of β and the refractive index n. Gaseous detectors, which have n close to 1, are most often used for PID in high energy physics. Other concepts involve multiple radiator types. To emit enough photons to determine a ring, the radiator length has to be sufficient. Due to continuous emission along the particle track, the 2D projection of the Cherenkov light forms a disc. Typically, a set of focusing and planar mirrors is used to obtain a ring and to project it onto a photon detection plane.

3.3 The LHCb RICH System: Current Status

The identification of charged hadrons, provided by the RICH system, is essential for the LHCb physics programme. The background of many b hadron decays can significantly be reduced with knowledge of the final state [33]. Figure 3.1 shows

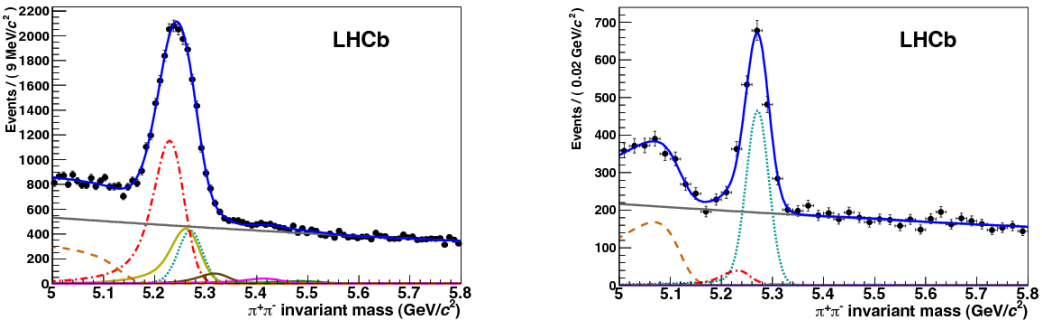

(a) (b)

Figure 3.1: Distribution of invariant masses for hadronic B decays, before including RICH PID information (a) and afterwards (b). The signal decay $B_d^0 \to \pi^+\pi^-$ is shown in dotted turquoise [34].

the decay $B_d^0 \to \pi^+\pi^-$ (turquoise line, dotted) as an example. The combinatorial background is shown in the grey solid line. The background of topologically similar decays, such as $B_d^0 \to \pi K$ (red line, dashed-dotted), $B_s^0 \to \pi K$ (brown line, dashed), or $B_s^0 \to KK$ (green line, solid) (Figure 3.1a), can be significantly reduced if information from RICH PID is included. The signal peak is separated from the background and a much reduced background from $B_d^0 \to \pi K$ remains (Figure 3.1b)

[34].

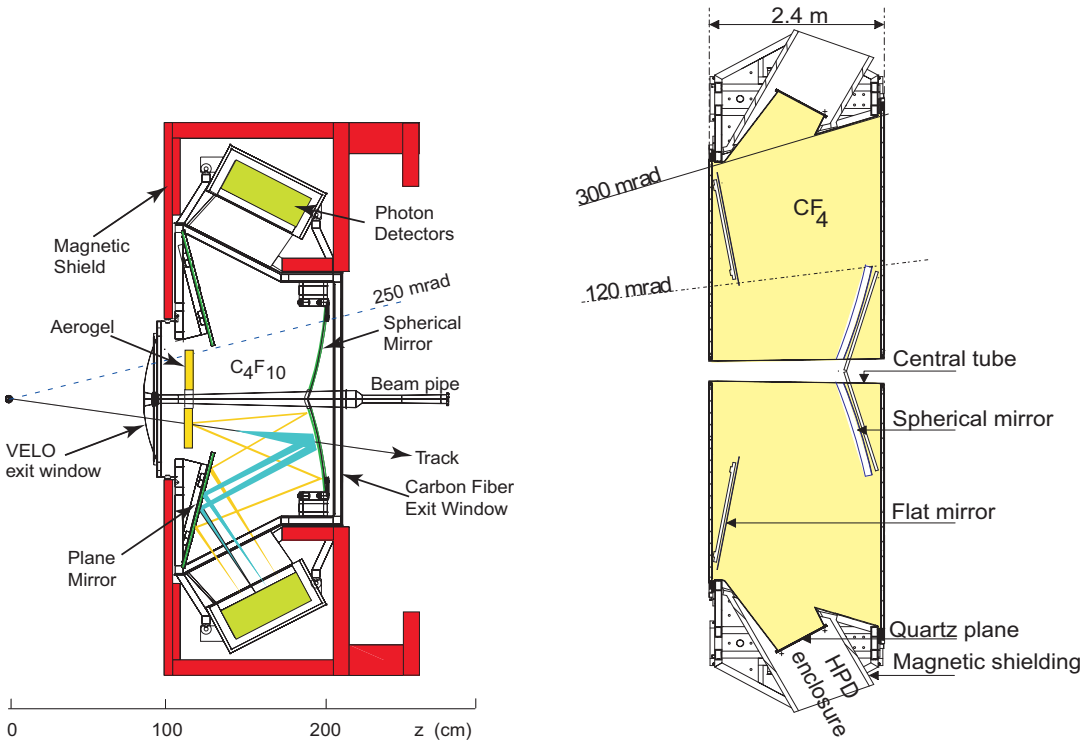

(a) (b)

Figure 3.2: Side perspective of RICH 1 during LHC Run 1, with Aerogel and C_4F_{10} as Cherenkov radiators (a) and top perspective of RICH 2 with CF_4 gas [4].

Figure 3.2 shows the design of the two RICH detectors in the Run 1 configuration, including the aerogel radiator. The properties of the radiators are summarised in Table 3.1.

The aerogel is a form of quartz (SiO_2) foam with very low density and low refractive index. It was installed to provide PID for low momentum particles with a lower threshold of 2 GeV/c for K. It was removed during the Long Shutdown I since its PID performance below the C_4F_{10} threshold was compromised by the high particle multiplicity in RICH 1 [22]. Without the aerogel, the C_4F_{10} radiator length is extended. Also, the combinatorics between photon hits and particle tracks was reduced by 50 %, increasing the reconstruction computing time significantly.

The measured Cherenkov angle is shown in Figure 3.3, for C_4F_{10} gas in RICH

	RICH 1		RICH 2
Radiator	**C_4F_{10}**	**Aerogel**	**CF_4**
L [cm]	85	5	167
n ($\lambda = 600\,\text{nm}$)	1.0014	1.03	1.0005
θ_{Ckv}^{max} [mrad]	53	242	32
$p_{thr}(\pi)$ [GeV/c]	2.6	0.6	4.4
$p_{thr}(K)$ [GeV/c]	9.3	2.0	15.6
$\langle N_\gamma \rangle$	32.7	6.6	18.4

Table 3.1: Properties of the LHCb RICH Cherenkov radiators

1, as a function of the particle momentum. One can see that π, K, and p can be clearly identified before saturating.

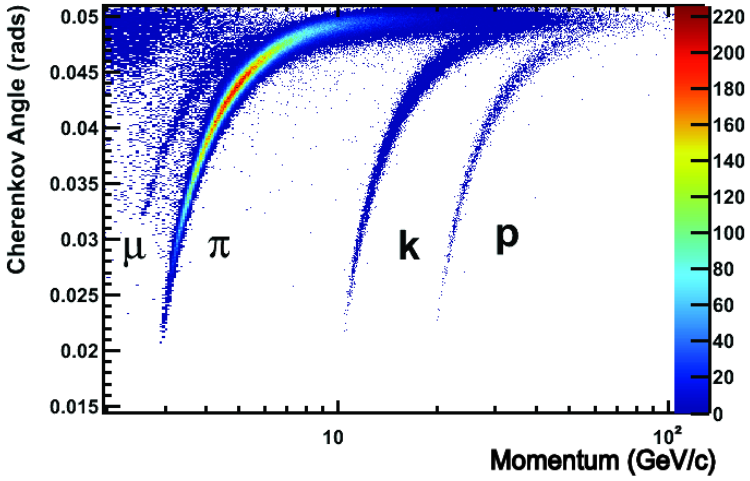

Figure 3.3: Reconstructed Cherenkov angle as a function of particle momentum for C_4F_{10} in RICH 1 [34].

3.3.1 RICH Hybrid Photon Detectors

As one can see in Figure 3.2, for both RICH detectors the Cherenkov light is guided by a system of two focusing and two planar mirrors to the two photon detection planes. The mirror system allows placing the photon detection plane away from the beam line, to reduce radiation damage. The spherical focusing mirrors form rings from the Cherenkov cones emitted by the particles. They are located inside the acceptance. To reduce multiple scattering effects in RICH 1, which is located upstream of the silicon tracking system, the mirror has a thickness of 2 mm and is

made of carbon fibre. Quartz windows seal the gas enclosure in the beam region and in front of the photon detection plane. For photon detection, Hybrid Photon Detectors (HPDs) are installed [35–38].

The Cherenkov photons detected by the HPDs installed in RICH 1 and RICH 2

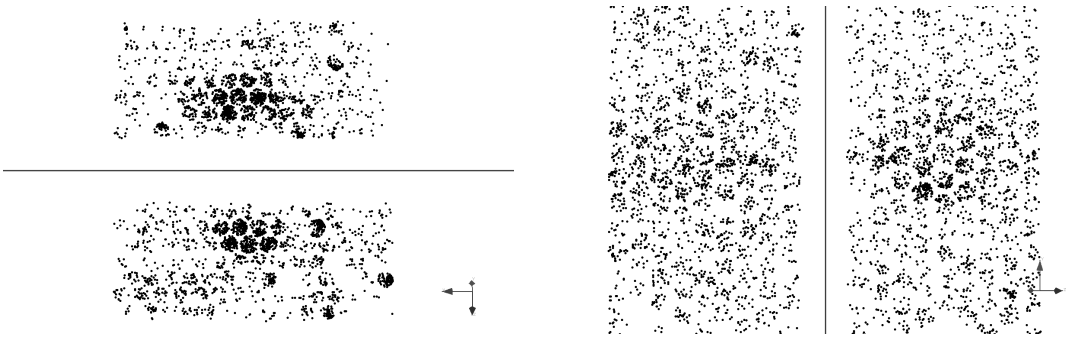

(a) (b)

Figure 3.4: One can see the Cherenkov photon hits on the circular-shaped HPDs for a typical LHCb event as seen by RICH 1 (a) and RICH 2 (b). The two photon detection panels are shown for the two detectors, respectively [2].

are shown as black dots in Figure 3.4 for a typical LHCb event. One can see the photon hits in the two vertically arranged HPD panels of RICH 1 (Figure 3.4a) and in the two horizontally arranged panels of RICH 2 (Figure 3.4b).

HPDs are custom designed to match the requirements of the LHCb RICH detectors: to detect Cherenkov photons in the wavelength range $200\,\text{nm} < \lambda < 600\,\text{nm}$ with a quantum efficiency larger than 25 %, low electronic noise, covering large areas (RICH 1: $1.2\,\text{m}^2$, RICH 2: $2.6\,\text{m}^2$) with 64 % active area, and to operate in a radiation environment of 3 krad per year and within the fringe field of the LHCb magnet. Figure 3.5a shows an HPD schematically and 3.5b a picture of the HPD panel in RICH 1, where HPDs are arranged in a hexagonal structure to achieve the largest possible active area.

HPDs integrate silicon pixel detectors and 1 MHz read-out electronics inside a vacuum tube. Photoelectrons are generated on the multi-alkali photocathode layer on the inner side of the quartz entrance window of the HPD, then accelerated through a single-stage $-20\,\text{kV}$ potential, and cross-focused onto pixels of size $500 \times 62.5\,\mu\text{m}^2$. The HPD tubes are surrounded by a mu-metal to shield against the field of the LHCb dipole magnet.

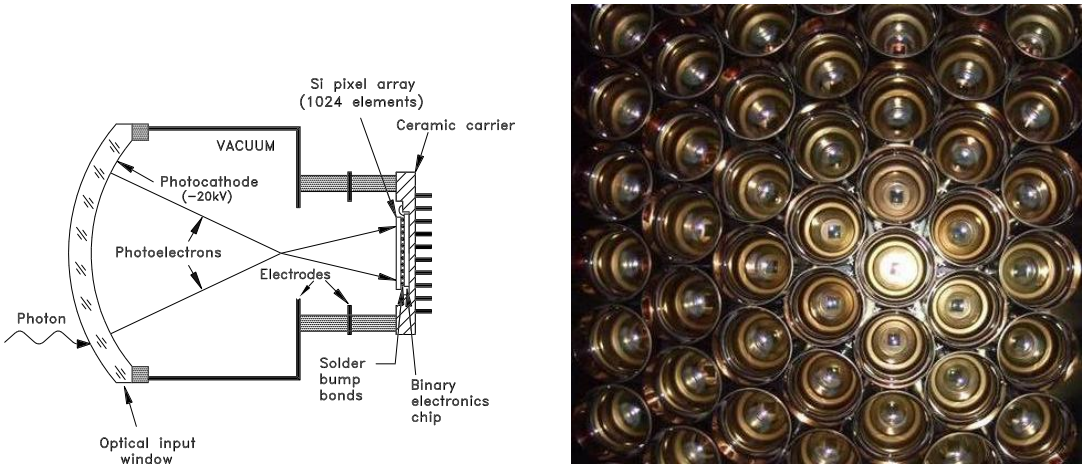

(a) (b)

Figure 3.5: Schematic of HPD (a) and picture of HPD panel installed in the RICH 1 detector [2].

3.4 The LHCb RICH Upgrade

To operate at the new instantaneous luminosity of $2 \times 10^{33}\text{cm}^{-2}\text{s}^{-1}$ starting in 2021 and to collect data at 40 MHz, the LHCb RICH system will undergo two major changes [25] during the two year Long Shutdown II of the LHC in 2019 and 2020. The optical components of RICH 1 will be adapted to the increase in occupancy and the entire photon detection system and read-out electronics of both detectors will be replaced [39–41].

3.4.1 RICH 1 Optical System Upgrade

The increase of occupancy in the central region of the RICH 1 detector would lead to a degradation of particle ID performance after the upgrade. To recover the performance, the optical system of the detector will be modified. This is achieved by a larger focal length of the focusing mirrors which increases the image area of the Cherenkov rings and therefore reduces the photon occupancy. The radius of curvature will change from 2710 mm to 3650 mm. The resulting change in tilt of the spherical mirrors also reduces aberration effects, which enhances the Cherenkov angle reconstruction. Additionally, the path length inside the radiator is increased which leads to a higher number of Cherenkov photons, further improving the reconstruction performance [40]. Figure 3.6 shows the RICH 1 optical system for LHC Run 2 (Figure 3.6a) and the modified system of Run 3 (Figure 3.6b). As a con-

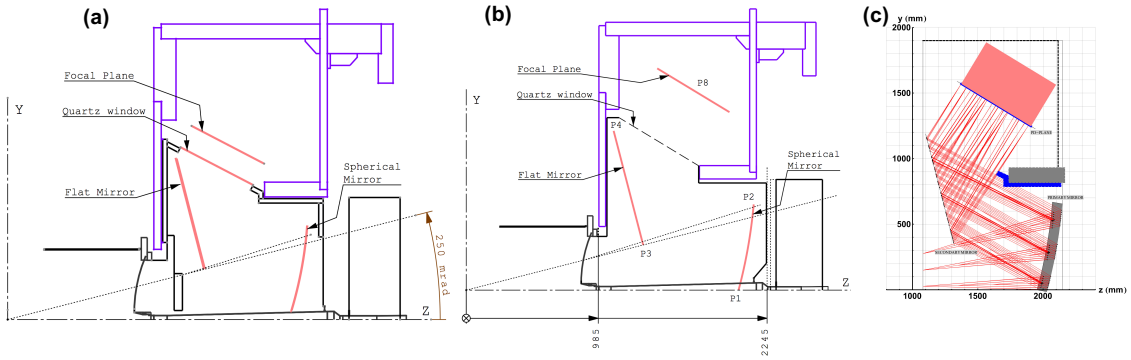

Figure 3.6: The current RICH 1 optical system is shown (a), as well as upgraded one (b). The radius of curvature is increased which results in a smaller spherical aberration and hence a better Cherenkov angle resolution. A larger radius of curvature and focal length of the spherical mirror increases the image area of Cherenkov photons and consequentially reduces the occupancy. As a result, the photondetection plane will be moved further away from the beam-line. A simulation of the photon path of the upgraded optical system is illustrated in (c) [39].

sequence of the larger radius of curvature of the mirrors, the detector plane will be moved further away from the beam-line. The simulated photon path is illustrated in Figure 3.6c. To keep the material budget inside the acceptance low, the spherical mirrors are made of a carbon fibre composite. The planar secondary mirrors are outside the acceptance and consist of glass.

3.4.2 RICH Upgrade Photon Detection System

Multi-anode PMT

Two types of Multi-anode photomultiplier tubes (MaPMTs) by Hamamatsu[1] will be used as new photon detectors for RICH 1 and RICH 2. The R13742 (R-type) and R13743 (H-type) are custom modifications of the commercial R11265 and R12699 series. The custom versions were adapted (e.g. in terms of gain specifications) to suit the purpose of Cherenkov photon detection within the LHCb RICH system, as a result of multiple test beam series since 2014 [42]. Both have 8×8 channels, the R-type has a size of $1 \times 1\,\text{inch}^2$ and represents the baseline for RICH 1 and high-occupancy regions of RICH 2 [43], with a geometrical acceptance of 77 %. The typical gain using a standard voltage divider exceeds 10^6 at 1 kV power supply [44].

[1]Hamamatsu Photonics: http://www.hamamatsu.com

The H-type has a lower granularity with a size of $2 \times 2\,\text{inch}^2$ and will be installed in low occupancy regions of RICH 2.

The MaPMTs are expected to operate for 15 years with an average data taking time of 1500 h/year. The gain of the MaPMTs is expected to degrade over time. It can be controlled by varying the potential of the photocathode or by threshold control using custom ASICs named CLARO [45]. Negative High Voltage (HV) will be applied to the photocathode while grounding the anode. The maximum supply voltage as stated by the manufacturer is $-1100\,\text{V}$.
The R-type features 12 metal channel dynode stages, whereas the H-type has 10 dynode stages. Both have a UV or borosilicate input window and bialkali photocathode [43, 46, 47]. A typical quantum efficiency (QE) curve for the R11265 MaPMT (corresponding to the baseline R-type MaPMT) is shown in Figure 3.7 for UV and borosilicate entrance windows, provided by Hamamatsu. The QE is slightly higher for borosilicate, however, less radiation hard than UV glass. After 630 kRad irradiation, the window transmittance decreases to 79 % for borosilicate in comparison to 93 % for UV glass [48].

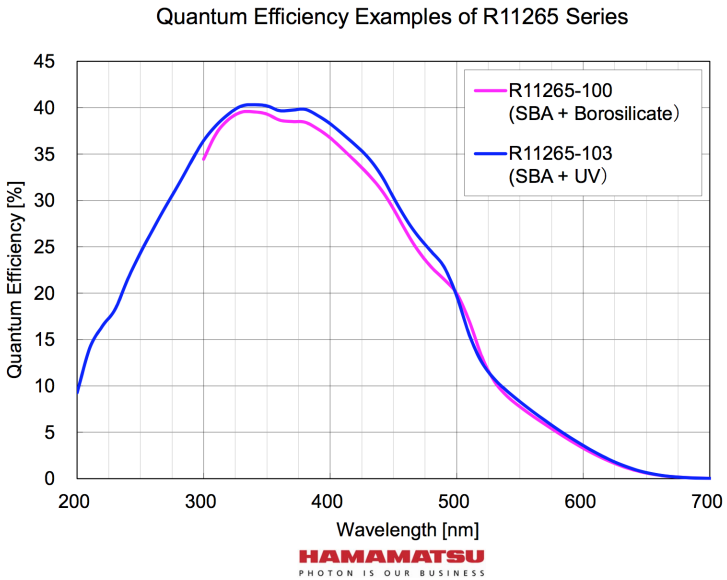

Figure 3.7: Quantum efficiency for the $1 \times 1\,\text{inch}^2$ R11265 MaPMT for UV or borosilcate entrance window as a function of wavelength [46].

Elementary Cell

The photon detector system and its electronics will be composed of autonomous functional units, called Elementary Cells (ECs) [48]. This facilitates detector assembly and maintenance, and provides flexibility of the geometrical arrangement of the photon detection planes, which was especially important in the early planning stages of the upgrade. This modular system allows efficient arrangement of the MaPMTs to increase the geometrical acceptance.

One EC contains either four R-type MaPMTs or a single H-type MaPMT, plugging into custom designed sockets which are located on a PCB, the Base Board. The EC is enveloped by an aluminium case which provides both structural rigidity and thermal transportation of heat to a cooling bar and serves as an electrical safety ground. The Base Board is connected to Front End Boards (FEBs), each of them containing eight 8-channel custom chips, named CLARO. An R-type EC houses four FEBs and an H-type houses two. The FEBs connect to the Back Board, which interfaces the FEB output to Digital Boards, which configure the CLARO chips and process signal events into Ethernet packets to provide them to the data acquisition system. An overview of the EC components is displayed in Figure 3.8a. A magnetic

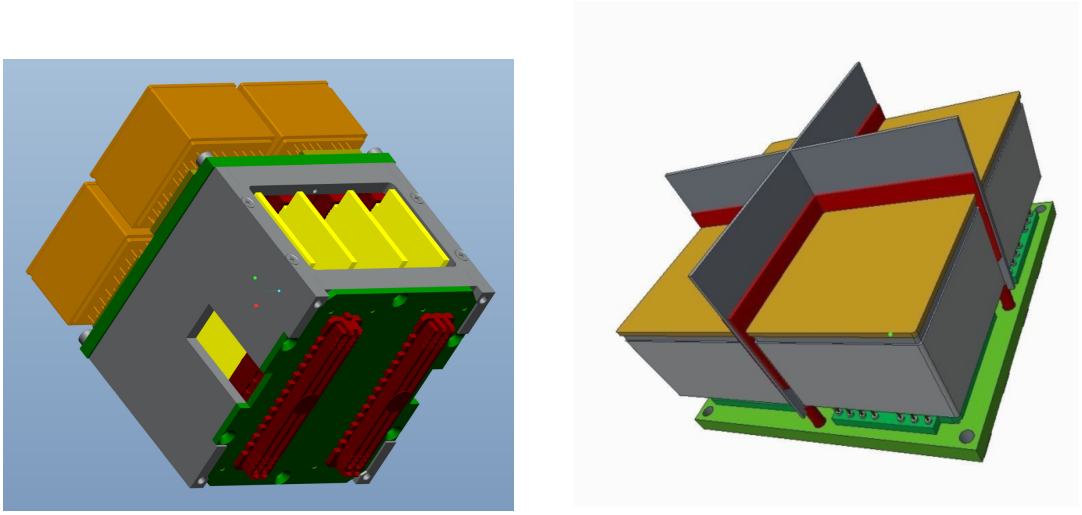

(a) (b)

Figure 3.8: Elementary Cell with four R-type MaPMTs (a). MaPMTs are shown in orange, Back Board and Base Board in green, the aluminium case in grey, the FEBs in yellow, and the sockets in red. The top part of the EC with a cross-shaped magnetic shield is illustrated in (b) [48].

shielding is currently under design, with a cross-shape for the R-type EC as shown

in Figure 3.8b as the most promising option.

The CLARO front-end chip consists of 8 channels with charge sensitive amplifier and discriminator to convert analogue current signals into digital voltage signals if a threshold is exceeded [45, 49]. This threshold can be individually set for each channel, allowing control of the signal to background ratio. This is referred to as the threshold efficiency.
The maximum expected event rate in the centre of RICH 1 is 40 MHz with an occupancy of 25 %. To operate in this environment, the CLARO is designed to recover the baseline in typically less than 25 ns.

4 MaPMT High Rate and High Occupancy Tests

This chapter depicts a study of the optoelectronic read-out chain of the MaPMT's performance at rates up to 20 MHz and occupancies up to 45 %. The nominal rate of 40 MHz was not subject to the investigation since the data acquisition firmware used in the prototype setup was not able to distinguish events at this frequency. An adaption of the firmware was not a priority since in the next series of test beam experiments the digital board prototype is going to be replaced by a new version. The obtained results allow extrapolating the effects of gain loss at 20 MHz to the nominal 40 MHz rate.

4.1 Experimental Setup

The test setup is depicted in Figure 4.1a. The two 8×8 channel MaPMT types, which are foreseen for the RICH Upgrade were tested. Two photon detection units (Section 3.4.2) are mounted on a cooling bar, which transports the heat away from the electrical components. The R-type EC (EC-R), comprising four 1 in R-MaPMTs, at the top position and a 2 in H-MaPMT (EC-H) at the bottom. The MaPMTs are mounted on a base board, which includes the voltage divider chain. Connected to the base-board are the Front End Boards (FEBs) onto which the CLARO ASICs [45] are installed. The CLARO chips are controlling pulse shaping and pulse discrimination. The latter part of an EC is comprised of the Back Board, connecting the FEBs to the Digital Boards (DBs). The DBs configure the CLARO chips and compress the events into Ethernet packets for the data acquisition system. For a detailed description of the MaPMTs and read-out electronics refer to the previous chapter, Section 3.4.2.

A schematic of the test setup is shown in Figure 4.1b. In two series of tests, first the EC-R and secondly the EC-H were placed in a light-tight box and illuminated

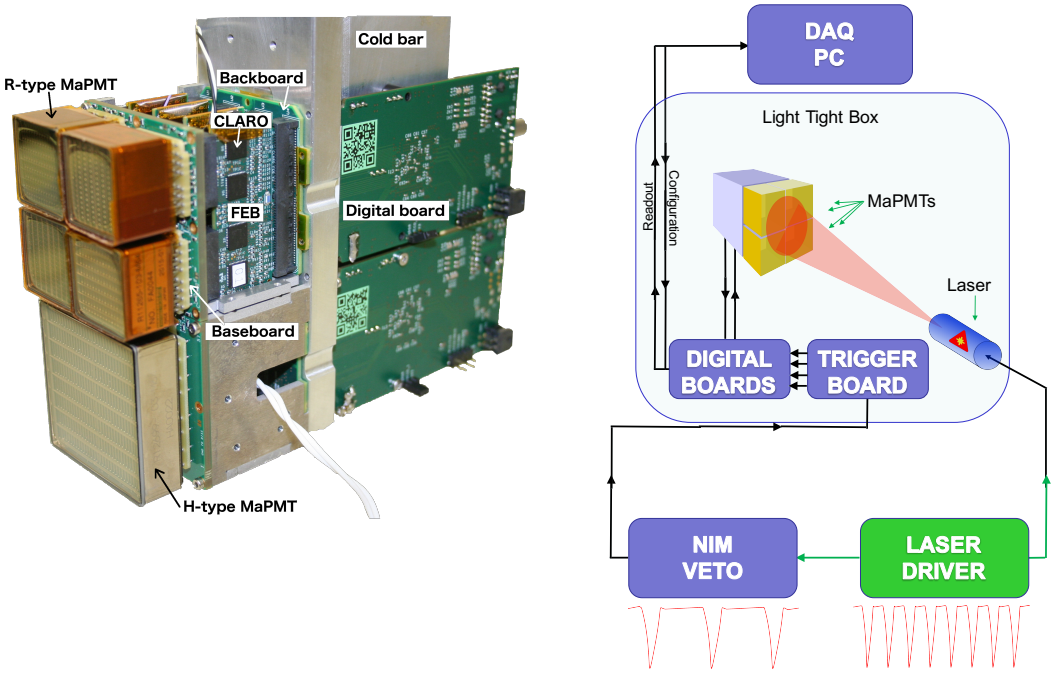

(a) R-EC and H-EC with digital boards. (b) Schematic of the test setup.

Figure 4.1: Picture of the cooling bar with R-type EC (top) and H-type EC (bottom) mounted, including digital boards (a). (b) schematically illustrates the test setup. ECs are illuminated by a pulsed laser inside a light-tight box. Laser driver and DAQ system are located outside the box [50].

by an ultrashort pulsed laser diode with a wavelength of 405 nm [51]. Rate and intensity were set by an external laser driver. The laser was coupled with an optical fibre aligned with the centre of the EC, causing a non-homogeneous illumination of the MaPMTs as shown in Figure 4.3, with high occupancies in the EC centre, decreasing towards the edges of the EC. This geometry was chosen to study a range of occupancies in the same run. The laser driver triggered the digital boards. A NIM veto was applied to reduce the trigger rate to 20 kHz, to reduce the data rate to the available bandwidth of th2e Ethernet connection between the digital boards and the DAQ computer. Since the system is running in a steady state, this only reduces the recording rate of events and does not affect the performance of the MaPMTs or the CLARO ASICs. Bias voltage was applied to the MaPMTs from a single power supply channel. The electric current of the supply was recorded to assess the

photoelectron current of the MaPMTs.

4.1.1 Pulse-Height Spectrum

To obtain the pulse-height spectra threshold scans were performed. After each 25,000 triggers, the threshold is increased. One threshold unit corresponds to a charge of about 35,000 electrons at the input of the CLARO. A feature to offset the threshold by 32 units was used to study the noise pedestal of the spectra in addition to the signal of photon events. Figure 4.2a shows typical threshold scans for 3 different R-type MaPMT pixels, as a fraction of the total number of triggers as a function of threshold units. For low thresholds below the pedestal, every trigger is counted. The sharp drop marks the pedestal position, after which the curve is dominated by the integrated photon signal. The steepness of the drop indicates that the noise level is below one threshold step unit. The fraction of signal counts per event after the pedestal drop, as shown in Figure 4.2a, was used to estimate the photon occupancy, which is varying due to the non-homogeneous illumination and individual gain of each channel. One can see the peak of the first photoelectron. The second photoelectron peak contribution is not visible since it occurs at higher threshold values and only in a small fraction of events relative to single photoelectron events.

To obtain the pulse-height spectrum, the distribution is fitted by two probability distribution functions (PDFs), PDF_{signal} and $\mathrm{PDF}_{pedestal}$, and one exponential function $\mathcal{E}$.

$$\mathrm{PDF}_{signal} = \mathcal{P}_1(\mu) \cdot \frac{1}{\sigma}\Big[1 + \exp(x - gain - x_{pedestal})\Big]^{-1} \tag{4.1}$$

$$+\mathcal{P}_2(\mu) \cdot \frac{1}{\sigma/\sqrt{2}}\Big[1 + \exp(x - 2 \cdot gain - x_{pedestal})\Big]^{-1} \tag{4.2}$$

$$\mathrm{PDF}_{pedestal} = \mathcal{P}_0(\mu) \cdot \left[1 + \exp\left(x - \frac{x_{pedestal}}{\sigma_{pedestal}}\right)\right]^{-1} \tag{4.3}$$

$$\mathcal{E} = \frac{A}{k} \cdot \exp(-k \cdot (x - x_{pedestal})), \text{if } x > x_{pedestal} \tag{4.4}$$

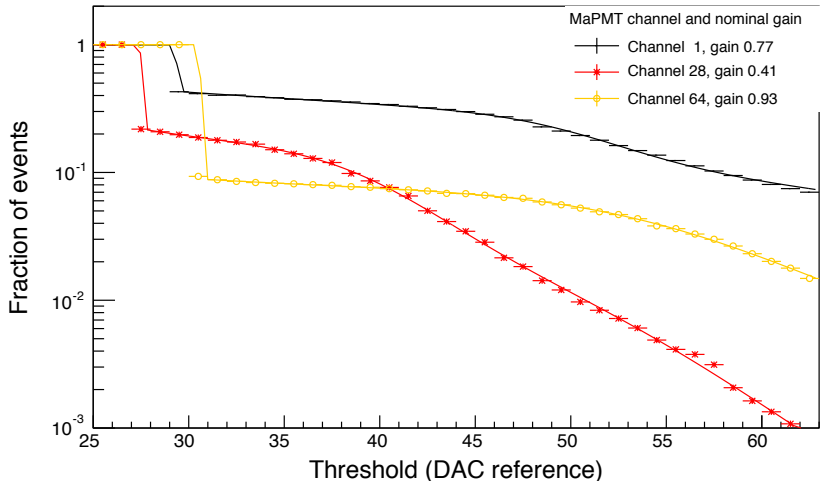

(a) Typical threshold scans for 3 pixels.

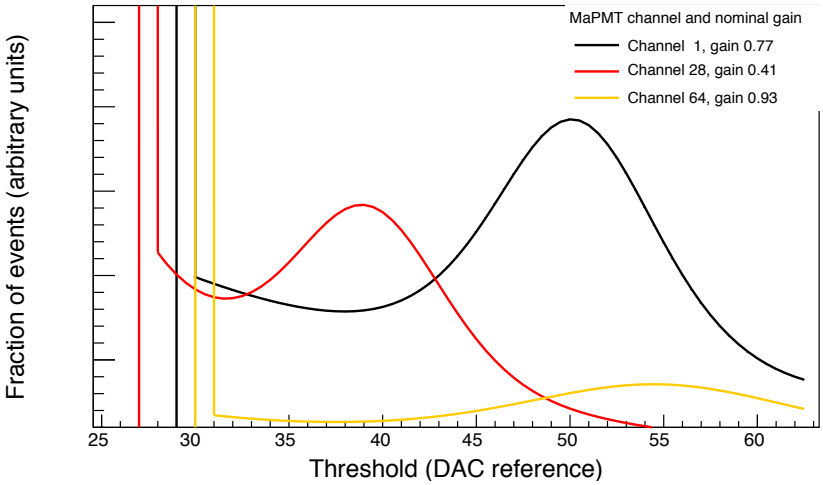

(b) Typical pulse-height spectra.

Figure 4.2: Typical threshold scans for 3 R-type MaPMT pixels with different gain (a). The fraction of events as a function of threshold units is shown. For low values, the pixels are always on. After a sharp drop, the signal is dominated by single photon events. This can be seen in the pulse-height spectra, which are obtained by fitting the threshold scan curves and differentiating the fit curve (b). The peak marks single photoelectron signals. A high gain results in a peak position at higher threshold values. Events with two photoelectrons are much less frequent and not visible in the given threshold range.

PDF_{signal} accounts for a single photoelectron and double photoelectron signal. These are described by Fermi distribution functions, which introduce the characteristic s-

like shape of the integrated spectrum in Figure 4.2a. The second PDF (Equation 4.3) describes the pedestal, also with a Fermi function. The Poisson PDFs $\mathcal{P}_k(\mu)$ are accounting for the normalisation between the zero (Pedestal), single, and double photon signal ($k = 0, 1, 2$, respectively). The exponential function $\mathcal{E}$ (Equation 4.4) is added to include the right-hand side tail of the pedestal. The tail is caused by dark counts and by photoelectrons which miss the first dynode stage. Due to the missing amplification, these electrons have a systematically lower gain, which overlaps with the pedestal.
The integrated spectrum is fitted by the sum of these three functions. The parameters of the fit are σ, μ (the average number of photoelectrons), $gain$, $x_{pedestal}$, $\sigma_{pedestal}$, A (normalisation of exponential), and k (coefficient of exponential). All seven parameters are free.
The fitted curve is differentiated, resulting in the pulse-height spectrum. An example of this procedure is shown in Figure 4.2b for the threshold scan curves of Figure 4.2a. The y-axis in this figure represents the derivative of the fraction of signal counts per laser pulse rate. One can use the pulse-height spectrum to characterise the pedestal position, gain, and noise of a channel.

4.2 Results

R- and H-type MaPMTs are studied at bias voltages of 900 V and 1000 V. The pulse rate of the laser rate is varied between 100 kHz and 20 MHz, corresponding to low and high intensities. The read-out rate is 20 kHz. The photocathode current is monitored as a function of pulse rates up to 40 MHz. Preliminary tests to power the last two dynode stages of the R-type MaPMT are presented, investigating the ability to stabilise gain and detection efficiency and to motivate further studies.

4.2.1 R-Type Characterisation

Figure 4.3a shows an occupancy map of the 4 R-type MaPMTs in the *low occupancy* test setting. Occupancy values reach nearly 30 % in the centre and decrease towards the outer area of the laser spot. In the *high occupancy* setting up to 45 % were reached in the centre. *Low occupancy* refers only to the comparison presented here, in the upgraded detector 30 % corresponds to the expected occupancy in the central region of RICH 1. The pulse-height spectra of a typical channel for 900 V and

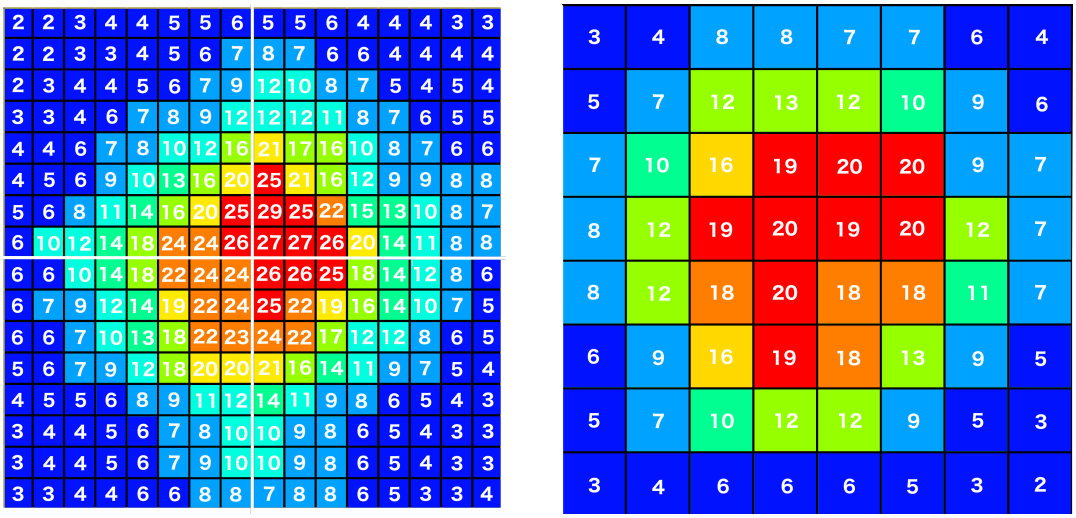

(a) Photon occupancy (%) map of R-type. (b) Photon occupancy (%) map of H-type.

Figure 4.3: Occupancy (%) map of 4 R-type MaPMTs for low occupancy test series (a), and for H-type (b). The laser is aligned with the centre of the EC, creating a spot with high occupancy values in the middle, decreasing towards the outer parts of the spot.

1000 V bias voltage are shown in Figures 4.4a and 4.4b, respectively. The effect is representative for all channels and shown for low and high occupancy settings.
One can observe, that the single photon peak position shifts towards higher threshold values with increasing laser rate and that the peak height is reduced by approximately 20 %, which indicates a lower photon detection efficiency.
If a large number of photoelectrons are produced due to a high occupancy, the resulting higher photocathode current increases the voltage at the first dynode stages. This increases the space charge density and causes current saturation [52]. This enhances charge amplification at the first stages, hence the gain increases with a high occupancy or laser pulse rate. The overall bias voltage is set by the external power supply and remains constant. As a consequence, the voltage at the last stages of the voltage divider chain decreases. The dynodes of the R-type MaPMT provide a large surface to reduce the signal density per unit area. They are arranged in close proximity to each other, leading to a higher electric field strength. The large peak signal current causes space-charge effects, which decrease the charge collection efficiency at the anode. The effect is much more pronounced at 900 V and for high photon occupancies. For 1000 V bias the effect is negligible. This can be explained by the raised electric field strength between the individual dynodes, which increases with the applied supply voltage [52]. The position of the pedestal is stable.

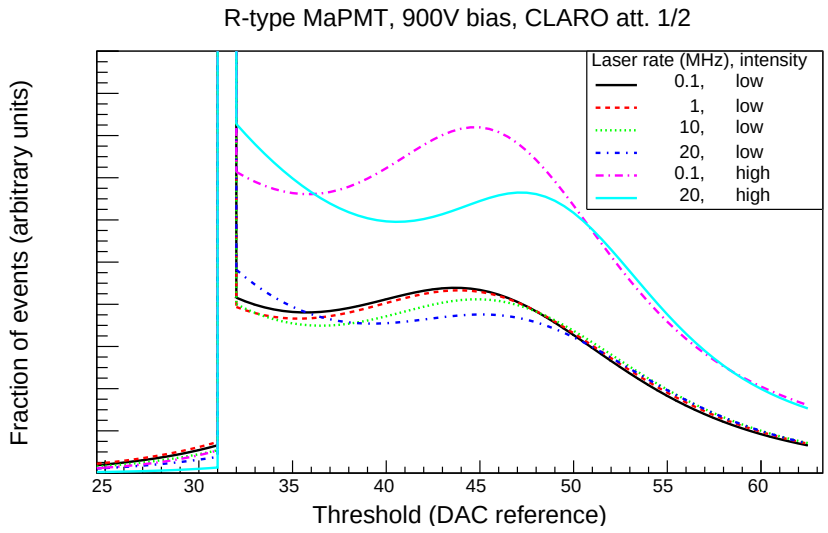

(a) 900 V pulse-height R-type spectra at low and high occupancies.

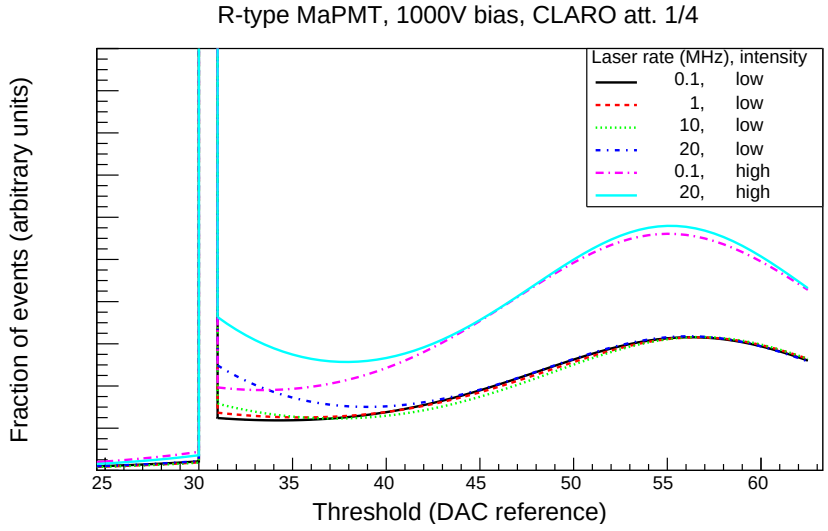

(b) 1000 V pulse-height R-type spectra at low and high occupancies.

Figure 4.4: Pulse-height spectra for R-type MaPMTs at low- and high-occupancy settings. The bias voltage was set to 900 V (a) and 1000 V (b).

4.2.2 H-Type Characterisation

A photon occupancy map for the H-type MaPMT is shown in Figure 4.3b. In the centre, occupancies up to 20 % were reached. This exceeds the expected value for the H-type MaPMTs, which are foreseen to be installed in the low-occupancy regions of the upgraded RICH detectors with less than 10 % peak occupancy [23]. To

account for the option of installing H-type MaPMTs in regions with higher photon occupancies with the benefit to lower the cost of the detector upgrade, the effect of occupancies up to 20 % on H-type MaPMTs is included in this study. One can see

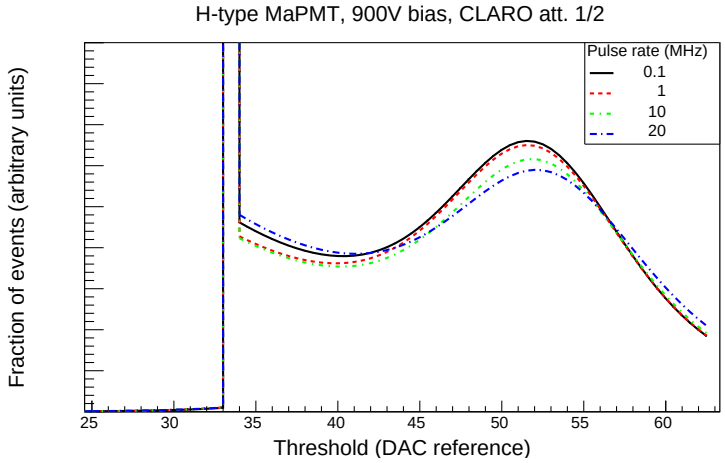

Figure 4.5: Pulse-height spectra for H-type MaPMTs at 900 V bias voltage.

in Figure 4.5 that the shift of the single photon peak is insignificant for increasing rates at 900 V. As for the R-type, the shift is even less pronounced and negligible at 1000 V bias. This can be explained by the dynode structure of the H-type MaPMT. Its larger dimensions allow for a lower signal density which reduces space-charge effects, resulting in a more stable gain and photon detection efficiency.

4.2.3 Photocathode Current

An external power supply was used to set the negative potential between the photocathode and the grounded anode, the corresponding electric current is referred to as the power supply current. The MaPMT current at the power supply was observed. It was converted into the electric current at the photocathode, using an LTspice simulation [53] of the voltage divider chain. Figure 4.6 shows the SPICE simulation that was used. The photocathode potential, which is set by the power supply, is denoted as *vPK*. The photocathode current is denoted as *iPK*. The potential at the last dynode stage is named *v12*, and the voltage at the second to last dynode as *v11*. These are set by the resistor chain to 10 % vPK and 16.7 % vPK, respectively.

Figure 4.7a shows the power supply current iPS (μA) as a function of photocathode current (pA), for bias voltages from 900 V to 1100 V in steps of 20 V, obtained from

the simulation. The 1.0 kV curve was used to convert from the measured iPS to iPK for different laser pulse rates. The option of powering the last two dynode stages to compensate a voltage drop was not used for this measurement. Figure 4.7b shows the photocathode current (pA) in dependence of the pulse rate (MHz) in the high occupancy setting. The pulse rate ranges from 100 kHz up to 40 MHz, for which is reaches a current of almost 100 pA. The limitation of the digital board to sample CLARO outputs only up to 20 kHz did not affect the measurement of the photocathode current, allowing to include the data point. The measurements show a linear increase of the photocathode current as a function of the laser rate within the error. This dependency allows estimating the photocathode current for different rates, ensuring to stay within the nominal maximum values provided by the manufacturer.

4.2.4 Powering of Additional Dynodes

As described in Section 3.4.2 the voltage divider chain of the MaPMTs consists of 12 dynode stages. The power supply delivers the bias voltage. A high intensity light signal causes a high current in the first dynode stages. To maintain the value set by the power supply, the voltage of the last dynode stages drops. This is expected to cause the observed increase of gain of the MaPMTs for higher rates, which is connected to the decrease in photon detection efficiency, as explained in Section 4.2.1. A preliminary series of tests has been performed for R-type MaPMTs with independent powering of the last two dynode stages. For that purpose, the Base Board of the elementary cell was modified to allow powering of the last two dynodes. Figure 4.8 shows a typical channel of an R-type MaPMT at 900 V with and without powering of the last two dynode stages. The voltages were set to 10 % and 16 % of the bias voltage for the last and second to last dynode, respectively. These values are given by the design of the Base Board as the ratio of the resistors in the stages, as shown in Figure 4.6 [48]. One can see that the shift of the single photon peak between 100 kHz and 20 MHz laser rate becomes insignificant when the last two dynode voltages are controlled by the power supply.

4.3 Summary

A high bias voltage improves the performance and gain stability of both the R- and H-type MaPMTs, which is caused by the enhanced electric field strength between the individual dynodes. At the same time, a high bias accelerates the ageing of the system. To increase the life-time of the MaPMTs and the overall photon detection system in the upgraded LHCb RICH system, the applied bias voltage is foreseen to be set to the lowest feasible value. The MaPMTs are expected to loose amplification gain over time, which will be compensated by increasing the bias voltage.
900 V bias voltage allows a good distinction between signal and electronic noise for the tested MaPMTs and represents an appropriate starting point for the upgraded RICH detectors. The optimal value has to be determined individually for each MaPMT. As the study shows, the gain at this voltage is not stable, especially for high photon occupancies and high event rates. The effect is significant for R-type MaPMTs at 900 V. At 1000 V the gain and efficiency remains sufficiently stable. The H-type MaPMT does not show a significant change for high rates and occupancies. To counteract the effect observed for the R-type MaPMT, a preliminary series of tests has been performed with powering of the last two dynode stages. The tests show a positive effect of individual dynode powering, substantially decreasing the single photon peak shift for high rates. This motivated further investigations during the LHCb RICH test beam experiment in October 2016. First analyses have shown that additional dynode powering has no adverse effect on the photon detection system [54]. To draw final conclusions on the effect of individual dynode powering on the signal region of the MaPMTs, further investigations are needed. The LHCb RICH Upgrade test beam experiment in June 2017 includes a dedicated tracking system which allows monitoring the beam intensity, which is a key requirement to reach a conclusion whether individual dynode powering is essential for the LHCb RICH detector upgrade to guarantee stable performance over the detector lifetime. Further tests are foreseen to investigate the possibility to power only the last dynode ($v12$), instead of the last two. This approach would reduce the complexity of the system for additional dynode powering. In addition, in June 2017, the feasibility to run the system with the *Photon Detector Module Digital Board* (PDMDB), has been demonstrated. The PDMDB will be used for the RICH Upgrade and is capable of taking data at 40 MHz, which will allow further tests of the photon detection system.

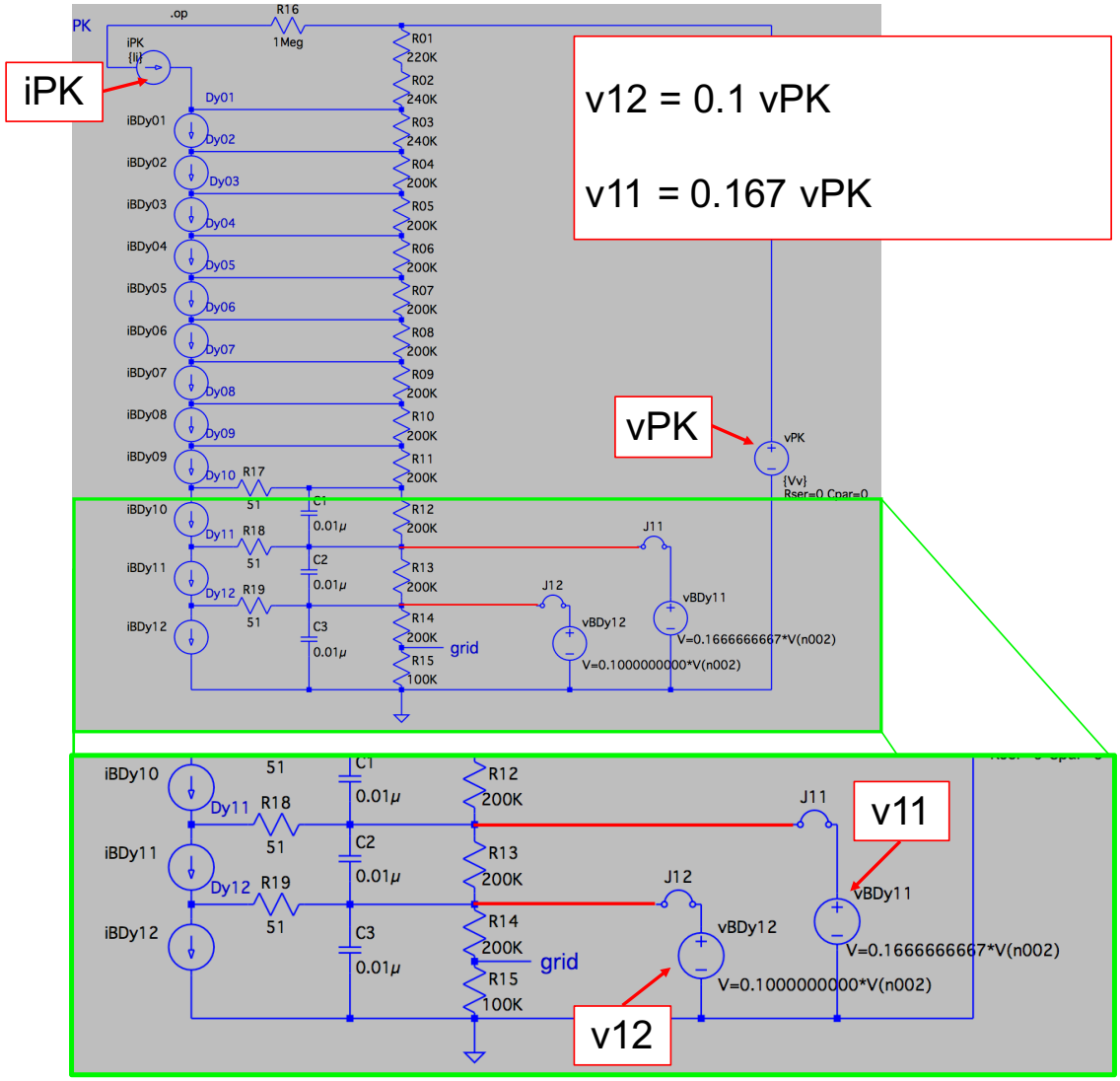

Figure 4.6: SPICE circuit of the voltage divider chain of the MaPMT. The section of the last two dynode stages with additional powering option is enlarged. vPK and iPK denote the photocathode voltage and photocathode current, respectively. The 12 dynode stages are shown. $v11$ and $v12$ represent the optional voltages for the last two dynode stages, provided by the power supply.

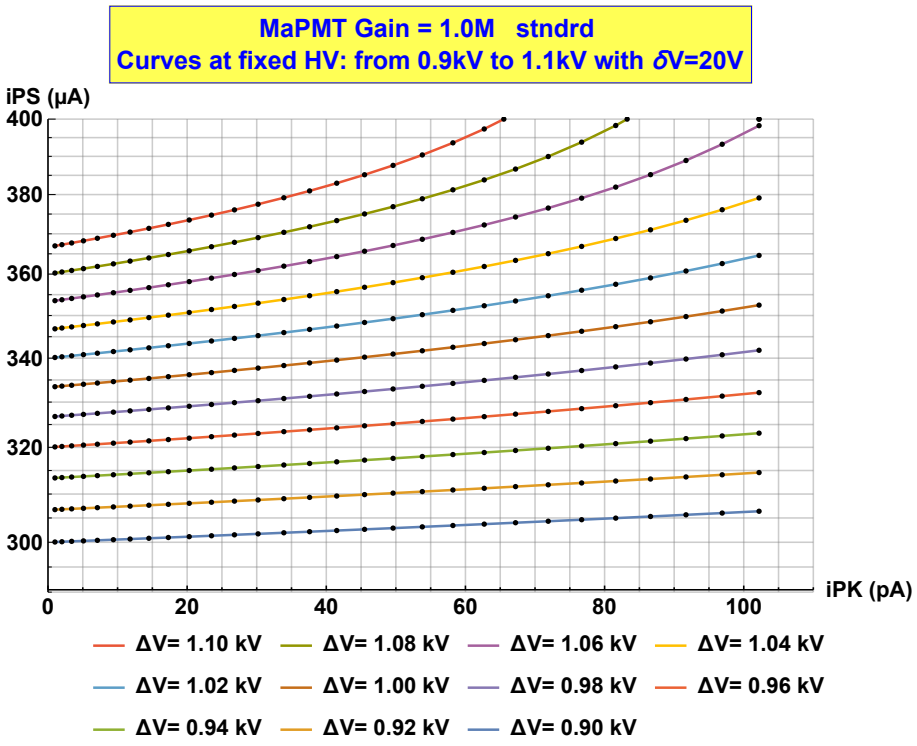

(a) Conversion from the SPICE simulation between photocathode current and anode current for various bias voltages.

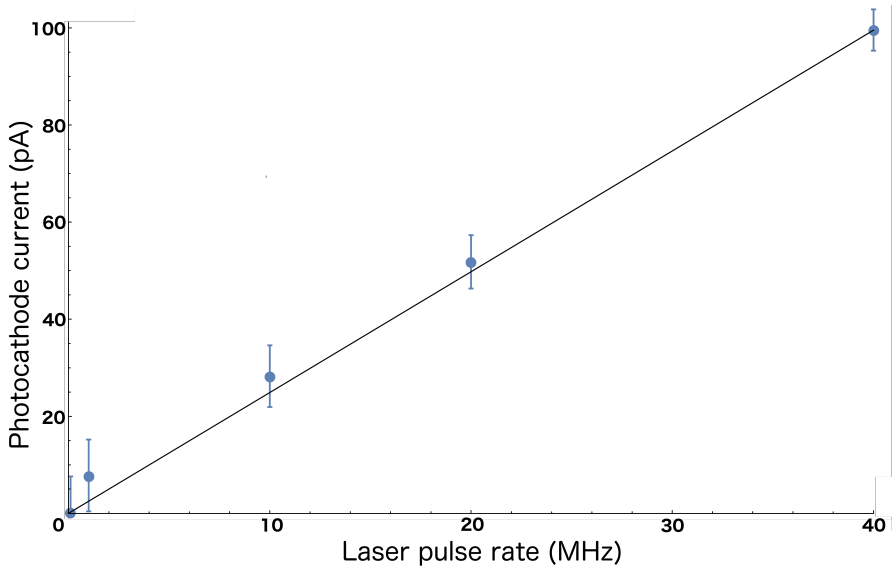

(b) Photocathode current as a function of the laser pulse rate. A linear dependence can be observed for rates from 100 kHz up to 40 MHz.

Figure 4.7: A circuit simulation (Figure 4.6) is used to convert between the measured anode current to photocathode current for different bias voltages ranging from 900 V to 1100 V in steps of 20 V (a) [48]. The anode current is shown on the y-axis in μA and the photocathode current on the x-axis in pA. The 1000 V bias curve, shown in brown, is used to plot the photocathode current as a function of the laser pulse rate (b). A linear dependence can be observed for rates from 100 kHz up to 40 MHz.

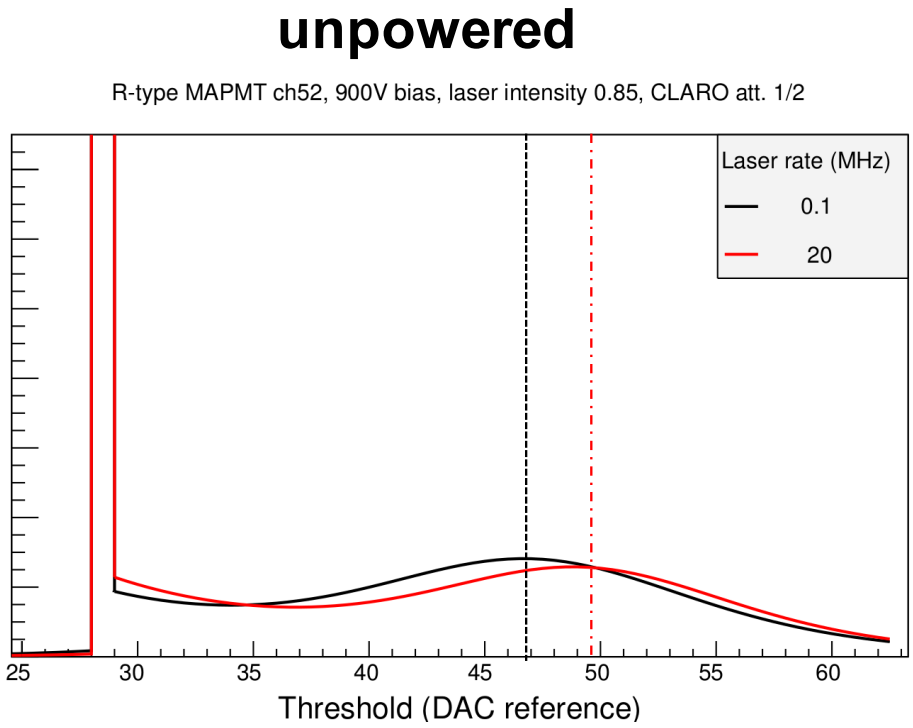

(a) R-MaPMT at 900 V without additional dynode powering.

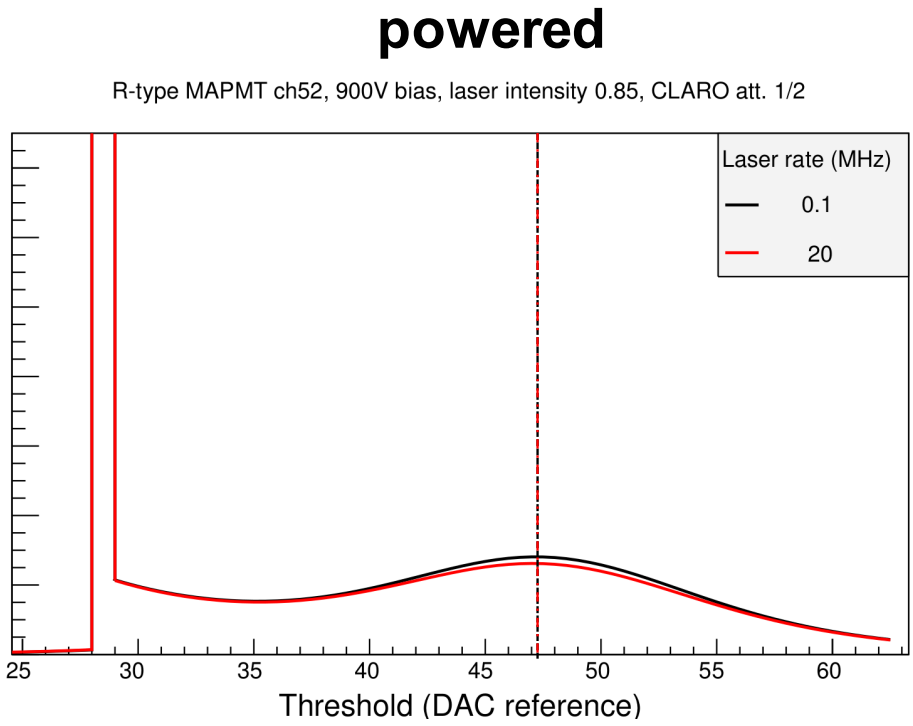

(b) R-MaPMT at 900 V with additional dynode powering.

Figure 4.8: Typical channel of R-type MaPMT at 900 V without and with additional dynode powering, Figures (a) and (b), respectively. For the two laser rates 100 kHz and 20 MHz a shift is visible without powering of the dynodes, and no shift with powering of the dynodes.

5 MaPMT Photon Yield Measurements

In this chapter, a study is presented that aims to validate data acquired in a test beam experiment for the LHCb RICH Upgrade. For this purpose, a full GEANT4 [55] simulation has been developed, based on an existing framework that was designed to simulate the RICH Upgrade test beam data acquisition chain of 2014 [42]. Using this simulation the total number of Cherenkov photon counts per incident beam particle will be compared with test beam data counts. This allows determining whether the photon detection system is characterised well in the simulation and whether its efficiencies are understood. To verify the validity of the photon yield comparison, characteristic properties of the Cherenkov ring, such as the Cherenkov radius, ring width, and the Cherenkov angle, are analysed for both simulation and data.

A reliable simulation of the optoelectronic chain for the upgraded RICH detector is crucial. It will eventually be used for the entire upgraded RICH detector, allowing to estimate the photon yield and the photon occupancy for certain regions and to compare these to measurements. Knowledge of these key features is mandatory to construct a detector with optimal particle identification ability.

In this chapter, the test beam experiment is described. An introduction to the GEANT4 simulation and reconstruction framework is given and the methods of comparison are explained. Finally, the results are presented in detail.

5.1 Test Beam Experiment

The RICH Upgrade test beam experiment was conducted over a duration of two weeks in October 2016. The goal of the experiment was to test the prototypes of the components of the optoelectronic read-out chain, as well as new powering schemes. The modifications comprised the possibility of additional powering of the last two dynodes to ensure a stable gain and efficiency at high rates, as a result of the study described in Section 4.2.4.

The goal of this study is to determine the photon yield of the MaPMTs in comparison

to the expectations given by a realistic simulation. Figures 5.1 and 5.2 show the

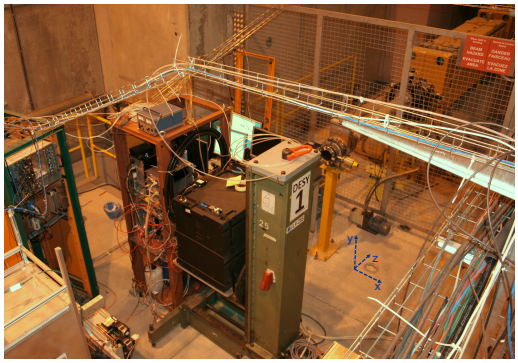

(a) Test beam area and light-tight RICH Upgrade test beam box.

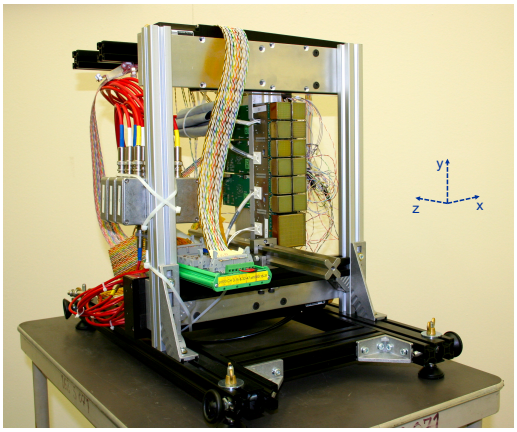

(b) Mechanical structure with 3 R-type ECs and 1 H-type EC.

Figure 5.1: Figure 5.1a shows the North Area of the SPS secondary beam for the LHCb Upgrade test phase in October 2016. The picture shows the upstream side of the light-tight box inside which the mechanical setup is installed. The box can be moved remotely in the plane orthogonal to the beam to align the setup with the beam. Figure 5.1b shows the MaPMTs in the mechanical frame of the test beam setup. 3 R-typeElementary Cells can be seen, containing 4 R-MaPMTs each, and 1 H-type at the bottom of the column.

test beam area (Figure 5.1a) and the mechanical frame, which holds the Elementary Cells (Figures 5.1b, 5.2a, 5.2b). To facilitate the comparison with the simulation which is described in the following section, the direction of the x-,y-, and z-axis are added to the pictures. In the simulation, the coordinate system origin for the xy-plane is defined as the centre of the borosilicate glass radiator lens, in which the Cherenkov photons are generated. The z-axis origin is in the centre of curvature of the radiator lens.

During the test beam data taking phase, the MaPMT configuration was varied. Unstable beam conditions allowed only one data set and MaPMT configuration to being studied. The MaPMT configuration of the data set which was used is shown in Figure 5.3. The small squares mark R-type MaPMTs and the large square marks the H-type. A schematic Cherenkov ring is illustrated in green. 10^6 triggered events were recorded in this configuration. This data will be compared to 10^5 simulated events, with the simulation sample size limited by computing time. The sample size of each of the data sets is sufficiently large to render the statistical error negligible

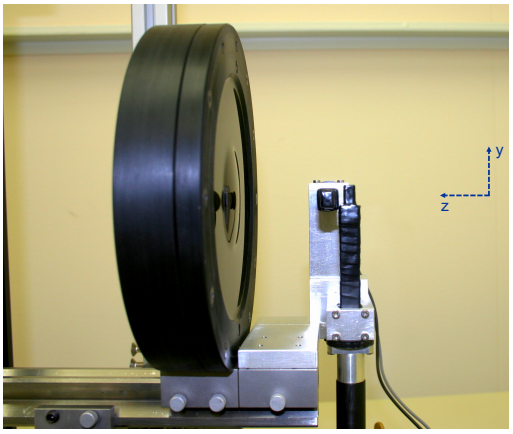

(a) Radiator and scintillators.

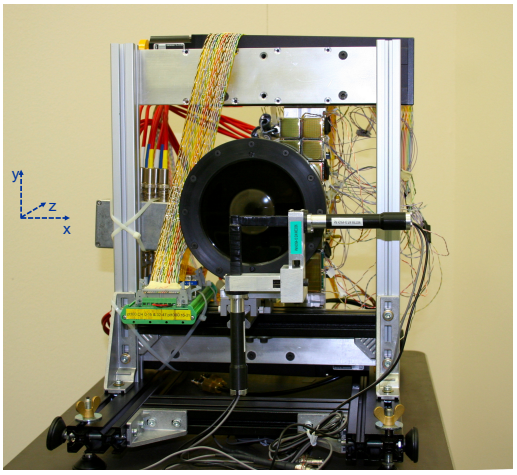

(b) Test beam setup with radiator.

Figure 5.2: The radiator lens is shown (a). On the upstream side two scintillators, which produce the trigger signals, are installed orthogonally. (b) shows the same mechanical structure as in Figure 5.1b, but with radiator and scintillators.

in comparison to the systematical uncertainty of the setup alignment. The relevant elements of the test beam experiment are described individually in detail in the following sections, ordered from up- to downstream as appearing in the test beam.

5.1.1 Particle Beam

The particle beam is a secondary beam originating from the Super Proton Synchrotron (SPS) at CERN. The protons hit a target, generating a beam of positive hadrons at 180 GeV. This hadron beam consists of protons (67 %), positively charged pions (30 %), positively charged kaons (3 %), and a small background of positive muons [1]. The beam arrives in spills of typically 10^5 to 10^7 particles over the duration of $3 - 5$ s.

The trigger signal is received by two orthogonal scintillators (Figure 5.2) inside the light-tight box. Each has a sensitive area of 8×12 mm, the overlapping surface area is 8×8 mm. A trigger signal is sent if both scintillators exceed a threshold within a pre-set time window. During data taking the LHCb VELO tracking telescope was also present in the area, located on the upstream side of the RICH setup with a distance of 1230 mm. The signal from the scintillators is sent to the telescope in order to be able to combine the data of the two setups. The information of the tracker

[1] Heinrich Schindler, personal communication, February 13, 2017.

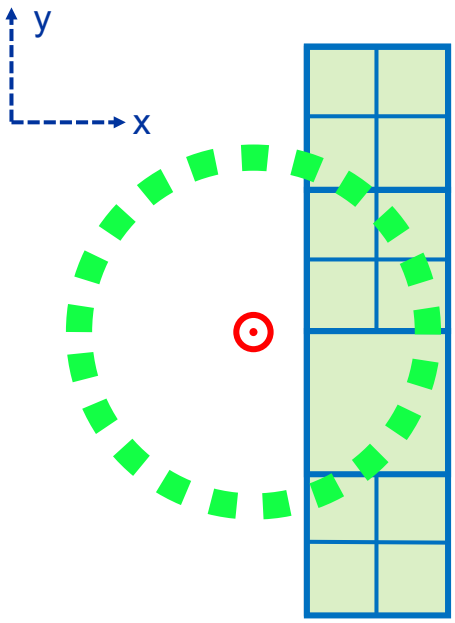

Figure 5.3: Downstream perspective schematic of MaPMT configuration. The red dot marks the beam position and origin of the xy-plane. The Cherenkov ring is illustrated in green.

contains beam profile and beam direction in the plane orthogonal to the beam. The beam width for triggered events is shown in Figure 5.4a. The total beam width exceeds the sensitive area of the scintillator triggers which causes a sharp cut of the beam profile. The beam direction is measured over the length of 75 mm, given by the first and last tracking stage of the VELO telescope, and displayed in Figure 5.4b in units of radian. The number of particle tracks counted by the telescope per event is presented in 5.4c on a logarithmic scale. One can see that the number of single-track events exceeds double-tracks by almost two orders of magnitude.

5.1.2 Cherenkov Radiator

The Cherenkov radiator, which is displayed in Figure 5.2a, serves both as a medium to create Cherenkov light and as a focusing lens. It is made of N-BK7 borosilicate glass and manufactured by *Edmund Optics* [56]. A schematic path of the photons generated in the lens is described in Figure 5.5. The particle beam traverses the radiator orthogonally, creating Cherenkov light, which is emitted under the material and velocity-specific Cherenkov angle θ_{Ckv}. Photons created in the downstream part of the radiator are absorbed by a circular-shaped, black coating on the flat surface

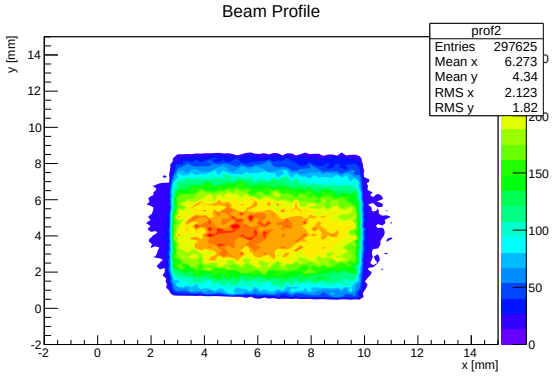

(a) Beam profile.

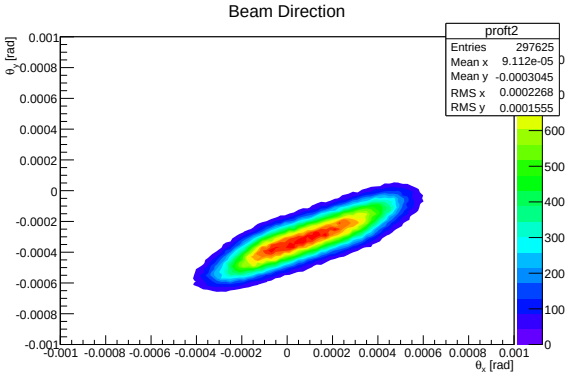

(b) Beam tilt.

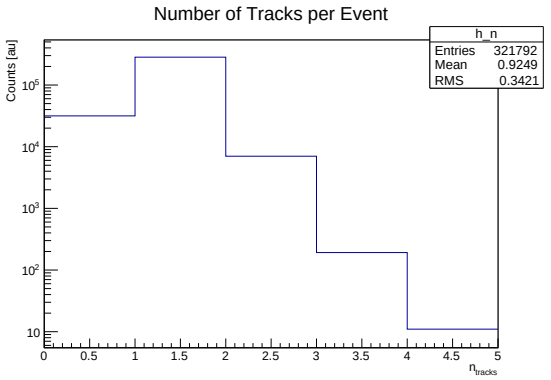

(c) Number of tracks.

Figure 5.4: On the top left one can see the beam profile as measured by the LHCb VELO tracking telescope (a). On the top right the x- and y-components of the angular tilt of the beam, with respect to the z-axis, is shown in radians (b). The histogram in (c) depicts the number of tracks per trigger event.

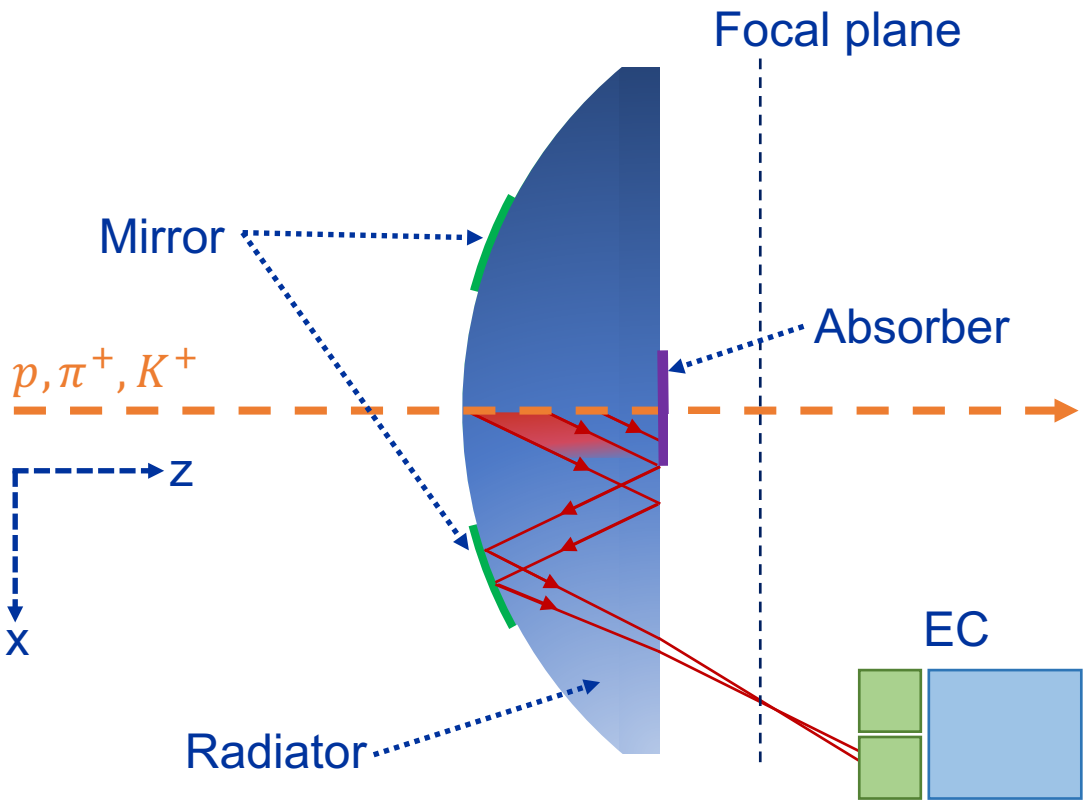

Figure 5.5: Schematic view of the radiator lens (top), elementary cell and particle path. Cherenkov photons are created symmetrically inside the radiator but drawn only on the MaPMT plane side for simplicity. Photons created in the first part of the lens are internally reflected on the flat surface, then reflected on the spherical-annular reflective coating and refracted when exiting the radiator. They hit the MaPMTs which are located behind the focal plane. Cherenkov photons which are created in the downstream part of the radiator are absorbed by a black coating.

of the lens. This feature was implemented for previous test-beam experiments to enhance the reconstructed Cherenkov angle resolution [42]. The Cherenkov photons which are generated in the first 12.5 mm of the radiator are internally reflected on the flat surface of the radiator and then reflected on the focusing mirror surface on the upstream spherically curved part of the lens. The reflective coating does not cover the entire spherical part but has an annular shape to minimise the reflection of background photons. The curved part of the lens is embedded in black silicon absorbing photons which do not fall onto the reflective coating. When exiting the radiator, the Cherenkov photons are refracted and hit the MaPMT plane. In the October 2016 test beam, the possibility has been exploited to install the MaPMTs

behind the focal plane of the mirror, hence creating a widened, defocused ring.

The test beam setup allowed moving the lens to achieve a focused ring, which would facilitate fitting a ring to compare circle parameters, as described in Section 5.2.2. However, this would also increase the probability of two photons hitting the same pixel. The digital signal would not be able to distinguish this from a single photon hit, which would bias the photon yield. The test beam data set of the setup in focused ring configuration was not usable due to misalignment between the SPS beam and the setup after reinstallation, not allowing a comparison between focused and defocused configuration.

5.2 The Test Beam Simulation Framework

The RICH test beam simulation framework was designed for previous test beam experiments in the past years [42]. It has been modified in terms of elements, geometry, material parameters, and reconstruction algorithms for the test beam analysis presented here. The structure of the framework is illustrated in Figure 5.6. The two main bodies of the framework are the simulation and the reconstruction module. Both use the same information about the test beam setup geometry and make use of LHCb software such as *Gauss* [57] and *Gaudi* [58]. To simulate particle interactions with the material of the setup, the GEANT4 toolkit is used. The material properties are implemented in the simulation as well. The output of the simulation is a list of MaPMT pixel hits for each event. The reconstruction part receives the list together with data from the test beam experiment which is combined with tracking telescope data. The reconstruction processes both simulation and test beam data.

5.2.1 Simulation

The simulation part of the RICH test beam framework is based on the GEANT4 toolkit. GEANT4 serves the purpose of generating the interactions of particles with matter. By default, GEANT4 includes a large variety of physics processes, which reduces computation speed significantly. To reduce computation time to a feasible level, a custom physics process list is implemented in this simulation. It includes **electromagnetic interactions**:

Electrons

- Multiple Coulomb Scattering

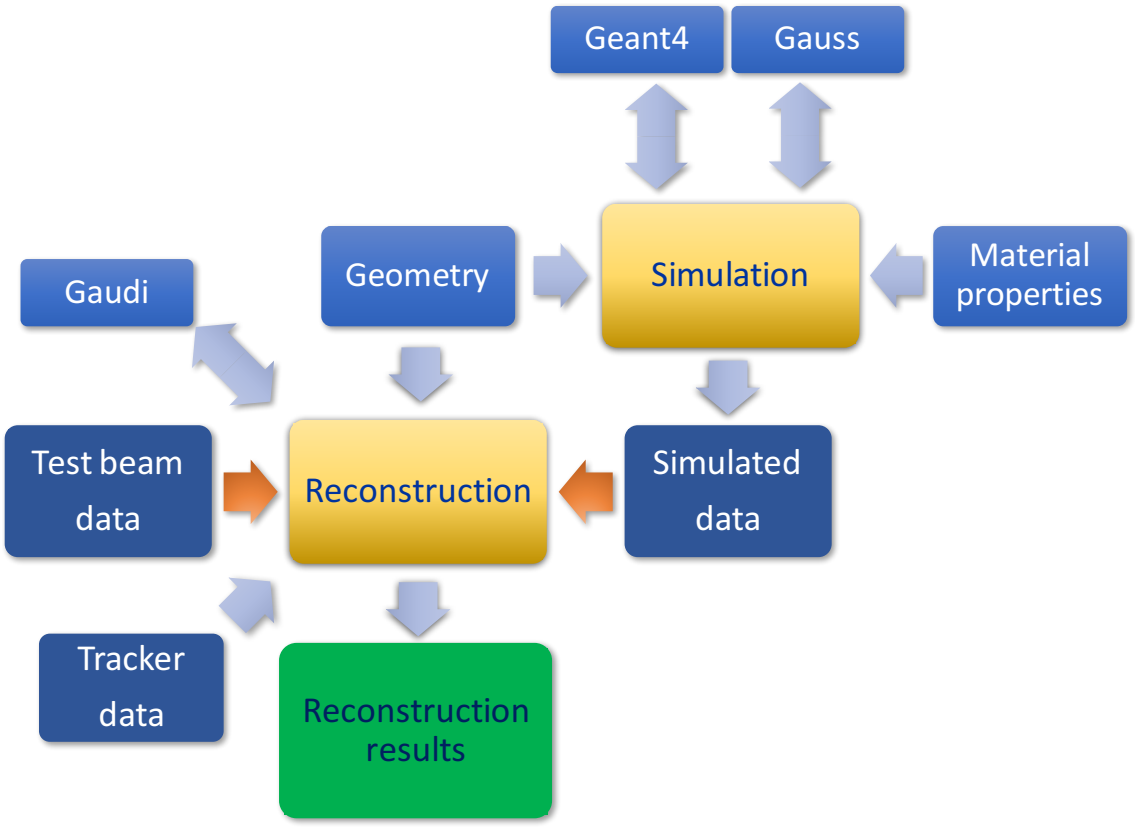

Figure 5.6: Schematic overview of the main features of the RICH test beam framework.

- Ionisation
- Bremsstrahlung
- e^+e^- - annihilation (for e^+)

Muons

- Multiple scattering
- Ionisation
- Bremsstrahlung
- Pair production

Photons

- Gamma conversion
- Compton scattering

Other charged particles

- Multiple Coulomb scattering

- Ionisation

For this study **optical processes** are of great importance. These include:

- Cherenkov radiation
- Scintillation
- Optical absorption
- Rayleigh scattering
- Photoelectric effect
- Boundary processes

The boundary processes include backscattering, absorption, and various reflection models (total internal, Fresnel, Lambertian, Lobe). It is important to note that GEANT4 distinguishes between gamma particles and optical photons. The latter are defined by their generation in scintillation or Cherenkov processes.
The simulation also includes the default particle decay processes of GEANT4. The physics processes are described in detail in the GEANT4 documentation [55].

Simulation Input

Particles are randomly generated around the z-axis on the upstream side of the setup. The beam profile was modelled to match the profile shown in Figure 5.4a using a Gauss function and cut-off for values larger than $\pm 8\,\mathrm{mm}$. The particles follow the direction of the z-axis with an energy of 180 GeV and particle composition of 67 % protons, 30 % π^+, and 3 % K^+. This follows the characteristics of the actual beam, neglecting the small beam tilt deviations depicted in Figure 5.4b.

A side view of the simulated setup is shown with and without beam in Figure 5.7. Only the radiator and the four ECs are shown, not the light-tight box. The radiator lens is centered on the beam line as shown, coloured in purple. The GEANT4 lens is generated by creating a cylindrical object with the radius of the radiator and a length corresponding to the length of the radiator along the z-axis. From this cylinder object, a sphere with sufficient width is subtracted, to match the radiator geometry specified in the manufacturer datasheet [56]. This procedure has been chosen instead of composing the radiator by combining the sub-volumes of a filled spherical cap and a cylinder, to avoid surface effects at the intersection of the

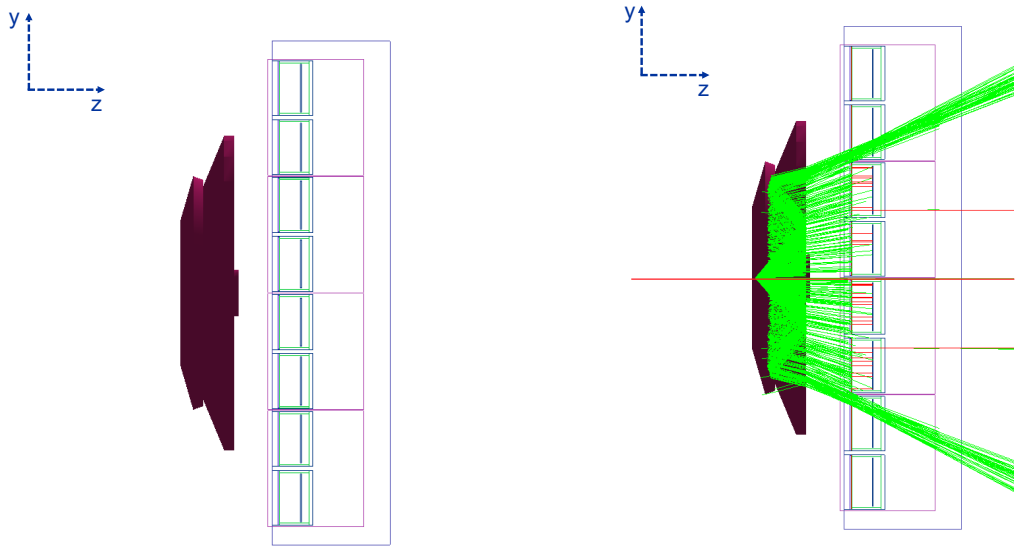

Figure 5.7: Side view of the simulated setup without beam (left) and with generated beam (right). For simplicity, only the radiator and four ECs are shown.

volumes. The volume on the upstream side of the radiator is the mirror surface which is in direct contact with the spherical side of the radiator lens. Similar to the experimental setup has a spherical-annular shape. On the flat part of the lens one can see the circular absorber.

Only a small number of high-energy particles is generated for this illustration. Their tracks are displayed in red. Cherenkov photons are displayed in green. The environment in- and outside the box is filled with air. The study focuses on R-type MaPMTs. Hence, for reasons of simplicity, four R-type ECs are simulated instead of three R-type ECs and one H-type EC as in the experimental setup. The data of the R-type EC which is in place of the H-type is not taken into consideration for this study. Hence, the reconstruction program receives the input of 12 R-type MaPMTs in total, both from simulation and data.

The measured quantum efficiency (QE) of each MaPMT is implemented into the simulation A typical QE curve is shown in Figure 3.7. Additionally, the threshold efficiency for each MaPMT channel is set to 98 %. This efficiency describes whether the electric signal originating from a photo-electron after going through the dynode chain of a MaPMT is high enough to be accepted. This also includes the capability of the electronics to detect the signal corresponding to the signal-to-noise ratio. The

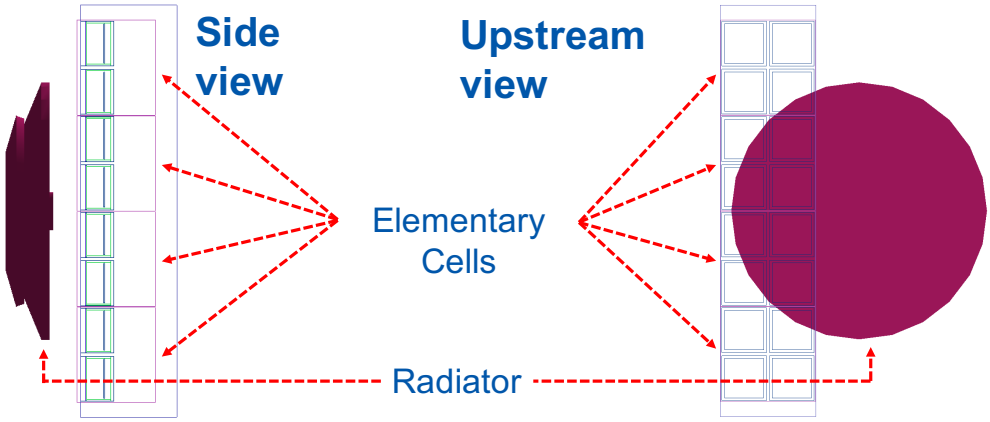

Figure 5.8: Radiator and MaPMT plane in the simulation from side perspective (left) and upstream perspective (right).

98 % threshold efficiency represents an average based on previous test beam studies [42]. Studies to determine the threshold efficiency for each channel individually are in progress and will eventually replace this average. These inputs represent crucial parameters concerning the general understanding of the photo-detection system. The high energy particles traversing the radiator volume create Cherenkov light in the characteristic angle θ_{Ckv} with negligible differences for the three particle types in the beam, due to their high energy and the defocused ring and the positioning of the MaPMT behind the focal plane. θ_{Ckv} depends on the wavelength following

$$\cos\theta_{Ckv}(\lambda) = [\beta \cdot n(\lambda)]^{-1}, \tag{5.1}$$

with $\beta = v/c$, where v is the speed of the particle. $n(\lambda)$ denotes the refractive index of the radiator lens as a function of the photon wavelength. This dependence, as well as the mirror reflectivity, was measured at CERN and provided to the simulation in form of a look-up table. The refractive index $n - 1$ of Cherenkov photons generated inside the radiator for the simulation is shown in Figure 5.9 as a function of the wavelength (nm). The reflectivity of the coating also varies with the photon wavelength. Similar to the refractive index of the radiator it is provided as a table to the simulation.

Simulation Output

The simulation program generates two output file formats, a CERN Root N-tuple and a text file. The N-tuple includes Monte Carlo information about the particle

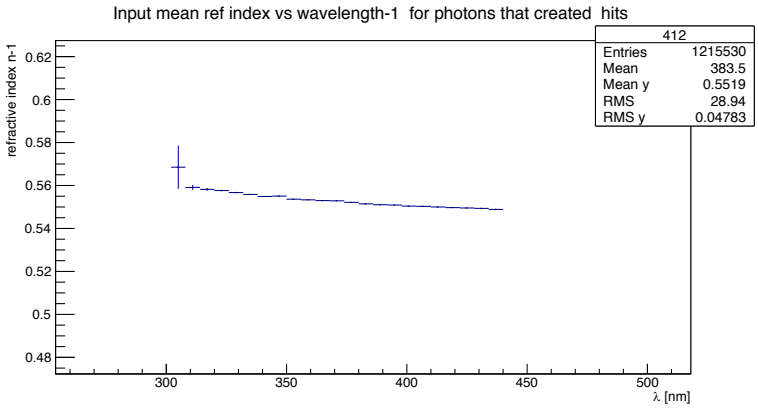

Figure 5.9: Refractive index $n - 1$ of the simulated radiator as a function of the photon wavelength in nm.

tracks generated in the simulation. This comprises beam particle type and direction, and exact hit position of the photon on the MaPMT plane.
The text file contains only the number of photon hits, the hit location, and MaPMT number, for each beam event respectively. That corresponds to the information available from the beam test data, to which it is compared in the reconstruction program part.

5.2.2 Reconstruction

The reconstruction part of the framework receives as input the data from the simulation, as well as test beam data. Test beam files are in the format of CERN Root TTrees. They include for each individual MaPMT the pixel number of the photon hits for each trigger event. Additionally, the LHCb tracking telescope, provides information on the beam direction, beam profile, and number of particles per trigger event, as shown in Figure 5.4.
For this analysis only events containing a single beam particle are included, representing the large majority of events as one can see in Figure 5.4c. This allows for a more precise comparison with the simulation results, eliminating the uncertainty of the number of particles per track for both, data and simulation.

Cherenkov Ring Fit

To compare the geometry and alignment of the simulated setup and experiment, as well as the physical properties of the components, the parameters of the defocused Cherenkov ring are determined for both data sets. For this purpose a fit of the ring on an event by event basis is implemented. The investigated parameters are circle centre position, ring radius, and ring width.
To allow for enough data points for the fit only events containing more than four photon hits in all MaPMTs combined are included. Events with more than 18 photon hits are excluded, since the high number of hits indicates the presence of secondary particles created in the radiator, creating further Cherenkov radiation and distorting the original ring fit.
The quality of a fit is determined an adaption of the standard deviation, given by

$$\sigma = \left[\frac{1}{n} \sum_{i=1}^{n} (\sqrt{(x_i - a)^2 + (y_i - b)^2} - R) \right]^{-\frac{1}{2}}, \tag{5.2}$$

where n is the number of data points, a and b the circle centre, and R the circle radius as determined by the fit, respectively.

Obstacles in fitting Cherenkov rings to the data arise from two facts. Firstly, the setup is asymmetric, as shown in Figure 5.8. The photo-detection system only captures a small arc. Data points are available only on one side of the ring in horizontal direction. The asymmetry in vertical direction is less pronounced since data points are captured on both sides of the ring centre in vertical direction. Secondly, the ring is defocused resulting in an intrinsic variation of the radius of the Cherenkov photons in addition to the resolution given by the MaPMTs.
These two problems increase the difficulty of finding a suitable fit curve. Drawing meaningful conclusions about the compliance of the simulated setup in comparison to the test beam setup is the goal of this section. Hence, the accuracy of determining the Cherenkov ring radius and centre has a higher priority than the efficiency of the fitting procedure.

Two approaches to fit the data were investigated, algebraic and geometric ring fits. Algebraic fitting methods are faster regarding computation time, but less reliable in determining consistent results. As an example for an algebraic fit, results of the

Taubin method [59, 60] are shown for data in Figure 5.10. The fit minimises the function

$$\mathcal{F} = \frac{\sum_{i=1}^{n}[(x_i - a)^2 + (y_i - b)^2 - R]^2}{\sum_{i=1}^{n}[(x_i - a)^2 + (y_i - b)^2]}. \tag{5.3}$$

The algebraic fit relies on the ordinary least squares method which minimises the

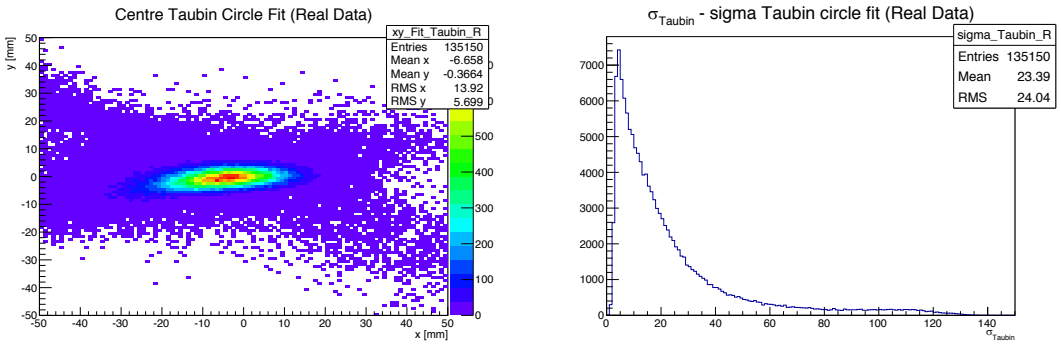

(a) Algebraic ring fit of data.

(b) σ of algebraic fit.

Figure 5.10: Algebraic circle fit of data. The fitted circle centre is shown (a) and the standard deviation of the fit (b).

sum of squared distance between a data point and the fit function. One can see from the very wide distribution of σ values in Figure 5.10b, that the algebraic fit in many cases does not describe the data well. This explains the widely scattered values for the circle centre in Figure 5.10a.
Geometric fits minimise the geometric (orthogonal) distances between fit and data points and follow the total least squares method. They are more suited for pattern recognition in graphical applications than ordinary least square methods [61] but have the disadvantage of higher computation time. However, they describe two dimensional data as provided by the experimental setup more accurately than algebraic fits, which can be seen from the distribution of σ for the geometric fit, shown in Figure 5.13c in the results section (Section 5.3.1), yielding much lower values and is narrower than for the algebraic fit.

The fit chosen for this analysis is described in Appendix B. It follows the geometric Levenberg-Marquardt method [62] and covers the full parameter space (a, b, R), with a and b as the circle centre position and radius R. The algorithm is implemented

following [60]. The goal of the fitting procedure is minimising

$$\mathcal{F}(a,b,R) = \sum_{i=1}^{n} [\sqrt{(x_i - a)^2 + (y_i - b)^2} - R]^2, \tag{5.4}$$

where n is the total number of two-dimensional data points (x_i, y_i), counted by index i.

Cherenkov Angle Reconstruction

In contrast to the circle fit, which is done for all detected photons in an event, the Cherenkov angle is reconstructed for each individual photon. Since the exact location of incidence of the photon on a MaPMT pixel is unknown for test beam data, the detection point is chosen with a flat random generator along the dimensions of the corresponding pixel. In the case of simulated data, the exact hit location is used for the reconstruction. The procedure to determine the Cherenkov angle is based on solving a quartic equation. It follows the principle of the algorithm used for particle identification in the LHCb RICH system [63].

A Cherenkov photon generated in the radiator follows the typical path illustrated in Figure 5.11. Photons generated after the first 12.5 mm of the radiator lens are absorbed by the cover placed on the flat side of the radiator. We approximate the photon generation point (E) in the middle of the 12.5 mm length. Since the angle of incidence at point R equals the angle of reflection due to total internal reflection, we can use E^* for the angle reconstruction. E^* is obtained by mirroring the emission point E at the flat surface of the lens. To determine the Cherenkov angle, the photon reflection point on the focusing mirror surface M has to be determined. We make use of the fact that M lies on the same two-dimensional plane as the centre of curvature (COC), E^*, and the detection point D. To facilitate the calculation we use information from the simulation to calculate the position of the detected hit without displacement due to refraction of the photon path D^*.
We obtain M by intersecting this plane with the spherical surface of the radiator lens. The calculation is described in detail in [63]. The intersection gives four solutions, two real and two complex ones. We discard the complex solutions. The second real solution is the reflection on the opposite site of the radiator, that would exist if it were a complete sphere. The intersection angle of the line between M and COC and the Z axis represents the Cherenkov angle θ_{Ckv}.

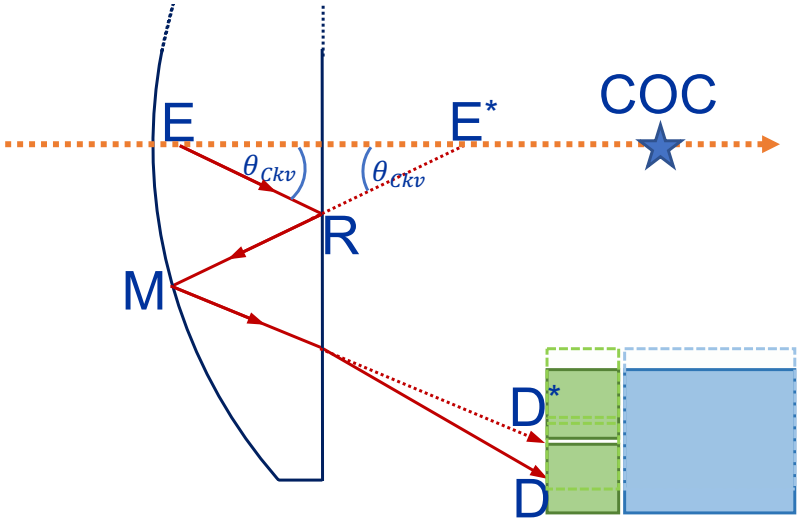

Figure 5.11: Schematic photon path with points used for the Cherenkov angle reconstruction: photon emission point (E), mirrored emission point (E*), total internal reflection point (R), focusing mirror reflection point (M), detection point (D), detection point without refraction (D*), centre of curvature of radiator lens (COC).

Photon Yield Fit

The number of detected photons is compared for each event and all MaPMTs simultaneously. Only events with a single incident beam particle per event trigger are taken into account for the test beam data, to match the simulation. The number of detected photons follows a Poisson distribution. To account for an additional particle that generates Cherenkov radiation (e.g. a secondary particle or an additional beam particle) the data is fitted by the sum of two Poisson distributions:

$$\mathcal{G} = c_1 \cdot \mathcal{P}_1(x, \mu_1) + c_2 \cdot \mathcal{P}_2(x, \mu_2), \tag{5.5}$$

where c_1 and c_2 are constants and $\mathcal{P}_{1,2}$ Poisson distribution, defined as

$$P_\mu(k) = \frac{\mu^k}{k!} e^\mu. \tag{5.6}$$

In this context μ is the mean value of the corresponding function and $k = 0, 1, 2, \ldots$ natural numbers. Since we are interested in the mean number of detected photons for a single beam particle, μ_1 of simulation and data will be used for the photon yield comparison.

5.3 Results

In this section, the Cherenkov ring centre, as obtained from the fit described in Section 5.2.2 of this chapter is compared, as well as the ring radius. The Cherenkov angle, obtained as described in 5.2.2 is also compared. The degree of similarity between these parameters in simulation and data is used to validate the simulation in terms of geometry, material parameters of the radiator lens, beam properties and physics processes.
In the next step, the photon yield of simulation and data is compared. A similar photon yield in simulation and data indicates that the efficiency values set in the simulation are representing the efficiencies of the photon detection system. We can make this deduction only after confirming that Cherenkov photons behave as expected, which we achieve in the previous step by comparing the Cherenkov ring parameters. If that is the case, we can conclude that both, in simulation and test beam experiment, a similar section of the Cherenkov ring strikes the photo-detector plane. This agreement dominates the uncertainty of the photon yield comparison. Other sources of uncertainties, such as the statistical process of Cherenkov photon creation in GEANT4 in terms of number and spatial distribution, are negligible [64, 65]. The reconstruction part of the framework receives data sets from both simulation and test beam experiment. A two-dimensional photon hit map is displayed in Figure 5.12. This allows a first qualitative analysis of the similarity of the two data sets. One can see that both ring position and width are well matching. The white area above the lowermost four R-type MaPMTs is where the H-type MaPMT was located while data taking, which is not included in this study. The white pixels are either malfunctioning or disabled due to high electronic noise which would bias the results. These are consequently disabled for both data sets.

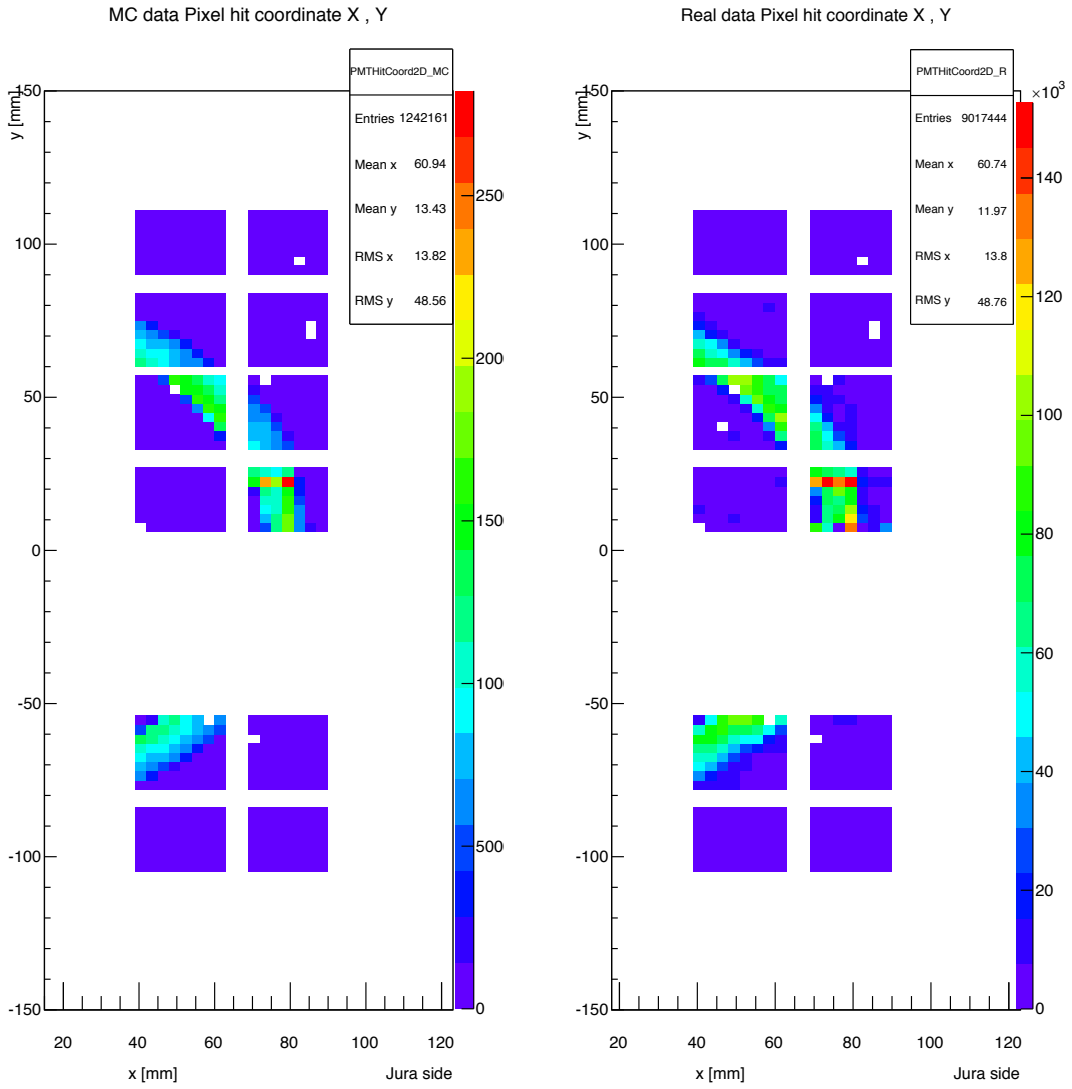

(a) 2D photon hit map simulated data. (b) 2D photon hit map test beam data.

Figure 5.12: Two-dimensional histogram of simulated data and test beam data, allowing a qualitative comparison.

5.3.1 Cherenkov Ring Characteristics

For a quantitative comparison in addition to the qualitative one, the ring fit described in Section 5.2.2 is applied for each triggered event. Only fits with $\sigma \leq 3\,\text{mm}$ (Equation 5.2) are included in the analysis. The distribution of σ is shown in Figure 5.13c. Figure 5.13 illustrates the two-dimensional distribution of ring centres in units of mm, as they were obtained by the fit described above. On the left-hand side,

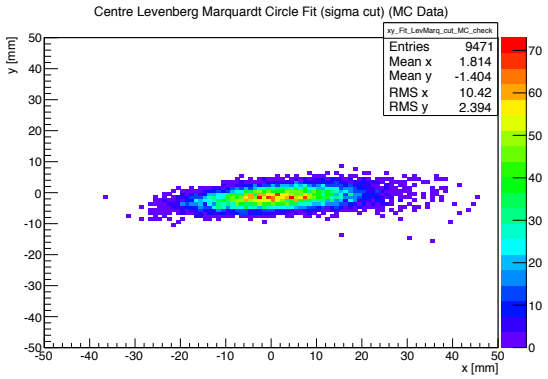

(a) Circle centre from simulation.

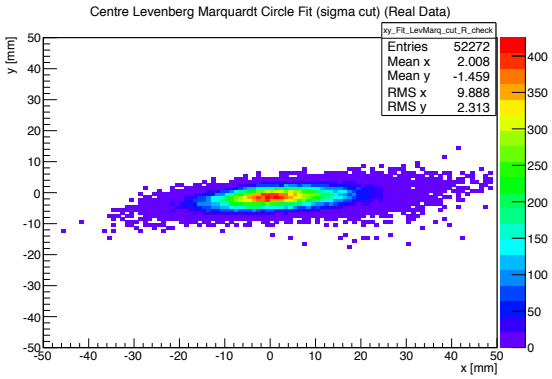

(b) Circle centre from data.

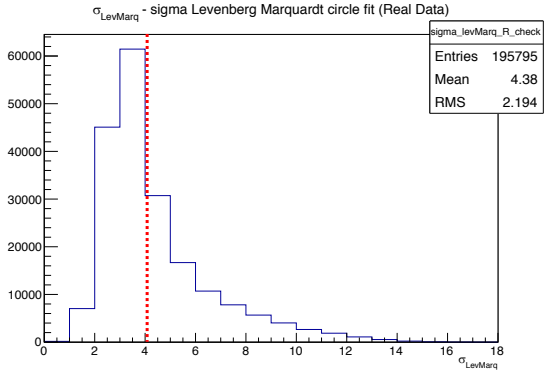

(c) σ of ring fit and cut.

Figure 5.13: Two-dimensional histogram of ring centre for simulation (5.13a) and data (5.13b), showing similar mean values with respect to the RMS. Figure 5.13c shows the goodness of the ring fit, measured by σ (Equation 5.2), shown here for test beam data. Only fits with $\sigma \leq 3\,\text{mm}$ are included in the ring parameter histograms.

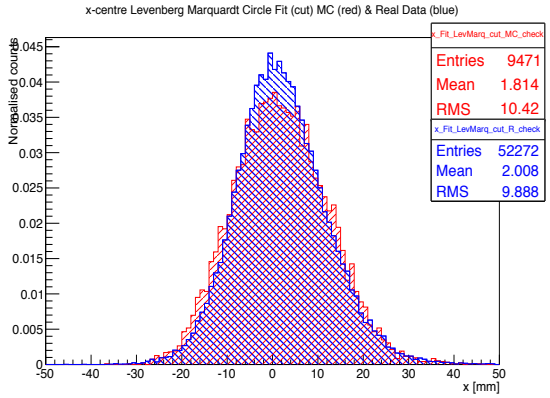

(a) Circle centre x-position.

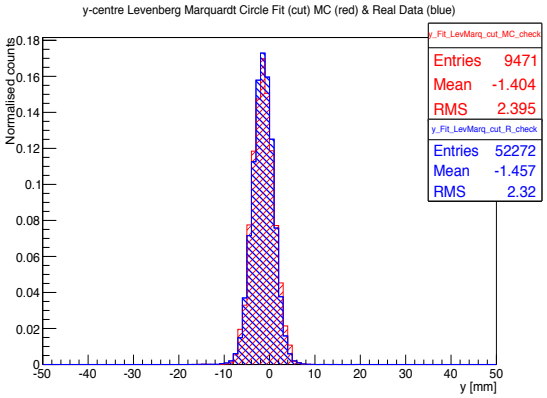

(b) Circle centre y-position.

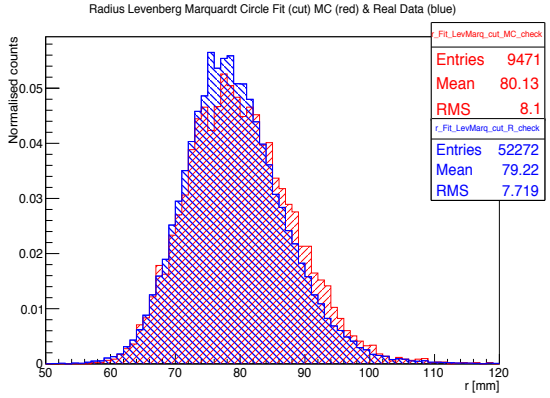

(c) Circle radius.

Figure 5.14: Cherenkov ring parameters of both simulation (red) and data (blue). The top two figures show the circle centre x- and y-components, the bottom figure shows the ring radius in mm. Both, mean values and distribution width are similar for all three parameters.

simulation results can be seen, the right-hand side shows the equivalent for data. The two components are depicted individually as normalised histograms in Figures 5.14a and 5.14b. Data is illustrated in blue and simulation in red. Additionally, the ring radius is shown in Figure 5.14c, also in units of Millimetres. The x-component of the fitted ring centre has a width of 10 mm, for both simulation and data. This is expected due to the setup asymmetry. The photomultiplier tubes are located only on one side in x-direction with respect to the radiator centre, as illustrated in figure 5.8. The y-component spread is narrower, about 2.4 mm, corresponding to the distribution of the MaPMTs along the y-axis. Two elementary cells with four MaPMTs each are located on the positive side of the y-axis, and one elementary cell on the negative side, providing data points on both sides of the ring centre, which increases

	$x_0[mm]$	RMS$_x[mm]$	$y_0[mm]$	RMS$_y[mm]$	$r[mm]$	RMS$_r[mm]$
Simulation	1.8	10	-1.4	2.4	80	8.1
Data	2.0	9.9	-1.5	2.3	79	7.7

Table 5.1: Summary of the mean values and distribution widths of the circle fit results, shown in Figure 5.14.

the precision of the fit. Another reason for the large distribution widths is the defocusing of the ring. This can especially be seen for the radius histogram, shown in Figure 5.14c. For a focused ring, the ring width is smaller than the MaPMT pixel size, in which case the pixel size is the dominating uncertainty [42]. The ring width in the setup studied here is larger than the pixel size. Consequently, the uncertainty in this comparison is dominated by the smearing of the Cherenkov ring.
The results of the Cherenkov ring fit are summarised in Table 5.1. The mean value of all three parameters agrees very well within the errors for simulation and data, as well as the standard deviations of the distributions. This indicates that the simulation matches the test beam setup in terms of geometry and generation of Cherenkov photons.

5.3.2 Cherenkov Angle

In this section, the result of the Cherenkov angle reconstruction is presented. It is reconstructed for each individually detected photon, as described in 5.2.2. One can

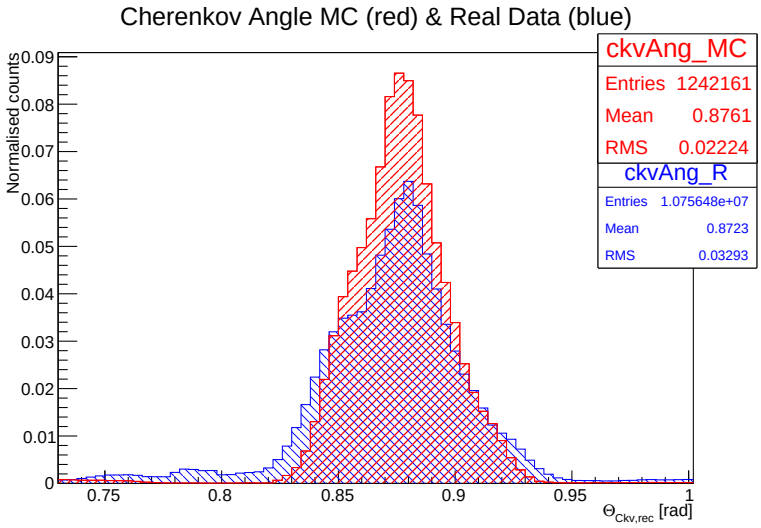

Figure 5.15: Reconstructed Cherenkov angle for simulation (red) and data (blue).

	$\boldsymbol{\theta_{Ckv}[mrad]}$	$\mathrm{RMS}_{\boldsymbol{\theta_{Ckv}}}\boldsymbol{[mrad]}$
Simulation	876	32
Data	872	49
Calculation ($n = 1.55$)	870	8

Table 5.2: Summary of Cherenkov angle values, obtained from simulation, data, and calculation (Equation 5.1).

observe a peaks with a shoulder towards smaller angles in the histogram, which we have not seen previously in the distribution of the Cherenkov ring centre and radius. This is resulting from reconstructing θ_{Ckv} for each individual photon, instead of an event-based fit as in the previous section. This allows comparing the two data sets with a different method. In Table 5.2 the mean values of the distributions are summarised. Also, the Cherenkov angle expected from the calculation for the average radiator refractive index $n = 1.55$ is shown, using Equation 5.1 and approximating $\beta \approx 1$ for 180 GeV beam particles. The RMS of the calculated Cherenkov angle is given by the refractive index range of the radiator, shown in Figure 5.9.

The comparison of the two normalised histograms lead to two main conclusions. First, they both peak at the same value and agree with the calculated angle within the margin of errors. They also show a similar structure of the main peak and a shoulder at values around 850 mrad. Secondly, the test beam data distribution is wider than the simulated one and features a tail towards smaller angles. Test beam data features a small number of photons with different Cherenkov angles, which are not present in the simulation.

We can draw two conclusions from these observations. The simulation implements the Cherenkov effect well enough to agree with data results and the expectations from the calculation. In the test beam, other particles than the main beam particles may generate Cherenkov photons in various directions.

Other physical processes, as scintillation, may also contribute. The properties of the radiator material borosilicate suppress scintillation effects, which indicates that the generation of secondary particles inside the radiator is more likely to be responsible for the excess in photons. These would have a lower energy than the primary particle, leading to smaller Cherenkov angles and consequentially to the described shoulder of the distribution. The deviation of potential secondary particles from the original beam direction would explain the larger width of the distribution.

Further beam particles which do not cross the trigger scintillators but coincide with the trigger window of a triggered beam particle would create a distorted Cherenkov

ring, since they do not cross the radiator lens in the centre, also contributing to a wider reconstructed Cherenkov angle distribution. These effects are not accounted for in the simulation. The reconstructed Cherenkov angle for simulated data is therefore showing a narrower distribution without long tails.

5.3.3 Photon Yield

From the previous two sections, we can conclude that the simulation represents the test beam setup in terms of position and properties of the components, as well as physical processes, such as Cherenkov photon creation.
As a final step, we will compare the number of detected photons per event, to investigate the photon yield of the detection system. With that measure, we can determine whether the photon detection efficiency of the optoelectronic chain is set correctly in the simulation. Figure 5.16 shows the number of photons detected by the setup per event, fitted to the sum of two Poisson distributions (Equation 5.5) for simulation (5.16a) and data (5.16b). Figure 5.16c features both histograms, where simulation is in red and data in blue.
The simulation peak value is at $\mu_{Sim} = 10.5 \pm 3.24$ and for data at $\mu_{Data} = 10.8 \pm 3.29$. The uncertainty is estimated by $\sqrt{\mu}$. The error of the minimisation, 0.01, is negligible.
We see that the distribution for data shows a long tail at high hit multiplicities, which is not present in simulation data. This substantiates our previous assumption, that secondary particles are generated more often in the test beam experiment, than in our simulation. The simulation is not able to take all processes into account which lead to secondary particles, without drastically increasing the computation time. That causes the entire distribution to shift towards lower values for simulated data. From the small area of the tail, we can see that this effect is not significant. It causes the surplus of 0.3 mean photon hits per event between for test beam data.
A similar background can occur when additional beam particles traverse the radiator within the trigger time gate without crossing the trigger scintillators. They are not hitting the radiator in the centre and create additional Cherenkov photons but with deviating reconstructed Cherenkov angle, since the reconstruction assumes the particles to traverse the setup in its centre.
The photon yield comparison shows that the simulated photon detection efficiency matches the efficiency of the optoelectronic chain in the test beam setup.

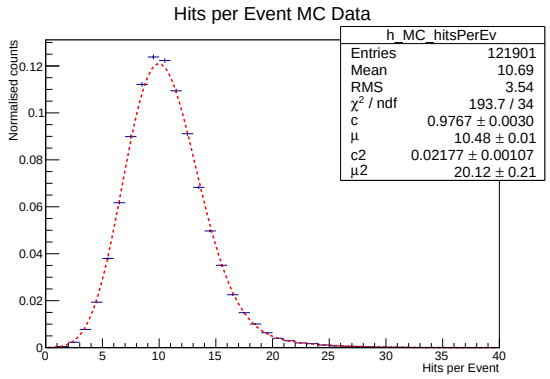

(a) Fitted number of hits per event from simulated data.

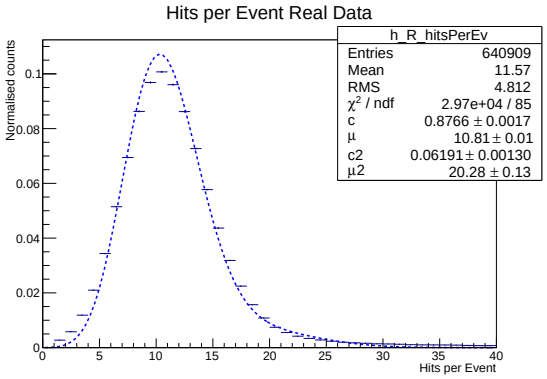

(b) Fitted number of hits per event from test beam data.

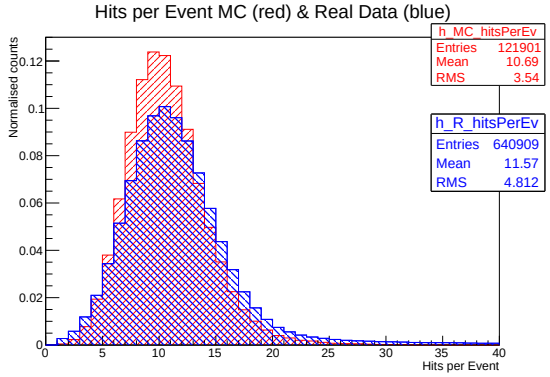

(c) Number of hits per event from simulated data (red) and test beam data (blue).

Figure 5.16: Histograms of the number of detected photons per event as a sum of all MaPMTs. (a) shows simulated data and (b) test beam data. Each is fitted by the function described in Equation 5.5. (c) shows both histograms overlapping, simulation in red and data in blue.

We compare this to an analytical estimate, following Equation 3.4. The wavelength range and refractive index is according to the Cherenkov photons generated in the radiator shown in Figure 5.9. Additionally, the following factors have to be taken into account:

- Average quantum efficiency $QE(\lambda)$ of the MaPMTs measured in the laboratory: (19 ± 2) %.
- Average transmission of the radiator measured in the laboratory: (94 ± 1) %.
- Geometric acceptance of the detected ring relative to the full ring: (22 ± 5) %.
- Dead area around pixel: (13 ± 1) %.
- Average reflectivity of mirror coating, approximated to be independent of the wavelength: (90 ± 1) %.
- Transmission coefficient at radiator-air interface, approximated to be independent of the wavelength: (96 ± 1) %.
- Average threshold efficiency: (98 ± 2) %.

The analytical estimate yields $N_{Calc} = 11 \pm 2.9$. The uncertainty is obtained by quadratic sum of the uncorrelated uncertainties of the factors listed above. The value N_{Calc} agrees within the uncertainty with the photon yield obtained from simulation and data.

The number of hits seen in the simulation shows that the photon detection efficiencies set in the simulation are accounting for the sum of detection losses in the experimental setup well. We do not see less detected photons in the simulation with respect to data, and we understand the source of excess in real data photon counts.

5.4 Summary

In this chapter, a simulation framework aiming for a description of the photon detection system for the LHCb RICH Upgrade was described. A detailed model of the experimental setup has been built with GEANT4 and validated comparing with test beam data.
To measure the similarity of the position of mechanical components, particle beam

and physical processes, the properties of the Cherenkov ring, such as Cherenkov angle, circle centre, radius and spread were analysed.
The ring position and Cherenkov properties confirm a good representation of the test beam set up in the simulation. This makes a photon yield comparison feasible. We can see that the simulation does not take into account all processes leading to the generation of photons. Taking into account all possible physical processes would not be feasible due to the consequential significant decrease in computing power. The effect is small enough to not bias the comparison of the photon yield. The mean photon yield agrees very well with simulated and test beam data. The efficiencies used in the simulation reproduce those of the experimental detection system to a good extent. We can conclude that the simulation is capable of representing the RICH Upgrade photon detection system and can be used as a foundation for the planned RICH Upgrade simulation framework.
For further improvement of the simulation framework, two main aspects should be considered. First, the threshold efficiency, which was set for all MaPMTs to 98 % as described in Section , should be determined for each individual pixel. This can be achieved by analysing the analogue photon spectrum of each pixel with respect to its individual signal threshold value. A study finding a procedure to reliably determine the threshold efficiency of a pixel from its pulse-height spectrum is under way.
Secondly, the alignment precision can be enhanced. The mechanical components should be set to a defined and fixed position in the laboratory, which allows higher precision than setting and measuring the position during the test beam experiment, in case the setup configuration is changed between different data sets. Additionally, aligning the tracking station mechanically to the light-tight box of the test beam setup would allow including the particle track direction in the reconstruction of the Cherenkov angle. This would give more insight into the agreement between Cherenkov photon generation in the simulation with respect to the real scenario. Future test beams are planned including an aligned tracking system to allow for this improvement.

6 Conclusion

The LHCb RICH system has proven in Run 1 and Run 2 of the LHC data-taking to be an essential element of the LHCb physics programme, by providing particle identification and thus significantly reducing the background in LHCb's most sensitive measurements. The goal of the LHCb RICH detector upgrade is to provide PID during Run 3 without deterioration in quality and reliability. To meet these conditions the optical system of the RICH 1 detector is modified, and the complete photon detection system of both RICH detectors including read-out electronics will be upgraded. To verify the performance of the new system under LHCb Upgrade conditions a series of studies and test beam experiments have been performed by the RICH Collaboration.

This thesis contributed to the RICH Upgrade performance tests with two studies of the multi-anode photomultiplier tubes (MaPMTs) which are foreseen as the new photon detectors.

The high-rate and occupancy capabilities of the two MaPMT types were tested in the laboratory. A single-photon pulsed laser was used to achieve occupancies up to 45 % for the $1 \times 1\,\text{inch}^2$ R-type MaPMT, and up to 20 % for the larger $2 \times 2\,\text{inch}^2$ H-type MaPMT, at laser rates up to 20 MHz. These values exceed nominal running conditions in terms of occupancy. The nominal 40 MHz rate was not reached due to limitations of the digital board, which is responsible for event processing. However, the consistency in results as a function of rate up to 20 MHz allows a conclusion to be drawn about the MaPMT performance.
At 1000 V bias voltage both MaPMT types operate reliably with stable gain and detection efficiency. To reduce stress on the system to ensure a long operation lifetime a bias voltage of 900 V is foreseen at the start of Run 3. At 900 V the R-type MaPMT decreases in performance, which is indicated by a shift of the single-photon peak in the pulse-height spectrum. The effect is negligible for the H-type MaPMT. To counteract the performance decrease of the R-type MaPMT at 900 V, prelimin-

ary tests of a modified dynode powering scheme were performed. The results of the preliminary tests suggest a significant improvement, motivating future studies.

A simulation was created using the GEANT4 toolkit to model the R-type MaPMT detection system in a test beam experiment. Data from the simulation and the test beam were analysed using a dedicated reconstruction program and analysis algorithms. The results of the analysis were compared to probe the similarity of the simulation to the real scenario. Close similarity was achieved in representing the test beam set-up and Cherenkov process with matching results for Cherenkov ring parameters and the reconstructed Cherenkov angle. The understanding of the detection efficiencies as determined by studies of the RICH Collaboration was examined by comparing the photon yield in simulated data and test beam data. A good agreement between the two data sets in terms of photon yield was found.

The studies confirm within their scope the suitability of the photon detection system which is foreseen for the LHCb RICH Upgrade. The simulation is capable of representing the baseline modules of the new system and to serve as a foundation for large-scale simulations of the upgraded RICH detectors. The results of the studies represent one further step out of many on the road to the successful upgrade of the RICH detectors, achieved by the Collaboration.

A List of Figures

B Appendix Circle Fit

The Cherenkov circle fit chosen for this analysis is described in detail below. It follows the geometric Levenberg-Marquardt method [62] and covers the full parameter space (a, b, R), with a and b as the circle centre position and radius R. The algorithm is implemented following [60]. The goal of the fitting procedure is minimising

$$\mathcal{F}(a, b, R) = \sum_{i=1}^{n} [\sqrt{(x_i - a)^2 + (y_i - b)^2} - R]^2, \tag{B.1}$$

where n is the total number of two-dimensional data points (x_i, y_i), counted by index i. To simplify the notation of the procedure we introduce

$$r_i := \sqrt{(x_i - a)^2 + (y_i - b)^2}, \tag{B.2}$$

$$u_i := (x_i - a)/r_i, \tag{B.3}$$

$$v_i := (y_i - b)/r_i. \tag{B.4}$$

The Levenberg-Marquardt method requires a set of formulae which are introduced in the following. We define the $n \times 3$ matrix

$$\boldsymbol{J} = \begin{bmatrix} -u_1 & -v_1 & -1 \\ \vdots & \vdots & \vdots \\ -u_n & -v_n & -1 \end{bmatrix}, \tag{B.5}$$

and the 3×3 matrix

$$\boldsymbol{N} = n \begin{bmatrix} \overline{uu} & \overline{uv} & \overline{u} \\ \overline{uv} & \overline{vv} & \overline{v} \\ \overline{u} & \overline{v} & 1 \end{bmatrix}, \tag{B.6}$$

containing the sample mean notation

$$\overline{x} = \frac{1}{n} \sum_{i=1}^{n} x_i, \tag{B.7}$$

$$\overline{xx} = \frac{1}{n} \sum_{i=1}^{n} x_i^2, \tag{B.8}$$

$$\overline{xy} = \frac{1}{n} \sum_{i=1}^{n} x_i y_i. \tag{B.9}$$

We define

$$\boldsymbol{g} = [r_1 - R, \ldots, r_n - R]^T \tag{B.10}$$

and compute

$$\boldsymbol{J}^T \boldsymbol{g} = n \begin{bmatrix} R\overline{u} - \overline{ur} \\ R\overline{v} - \overline{vr} \\ R - \overline{r} \end{bmatrix}. \tag{B.11}$$

The diagonal components of the matrix $\boldsymbol{N}$ are varied by parameter λ. This control parameter, and hence the variation, is usually chosen to be small for the first iteration of the algorithm. For this study, the parameter was initialised as $\lambda = 10^{-2}$. This initial value proved to lead to fit convergence in fewer iterations than 10^{-1} or 10^{-3}. After one complete iteration of the algorithm, the control parameter λ is adapted to the results of the iteration. It is either decreased by parameter α or increased β. The adaption parameters were set to $\alpha = 0.1$, and $\beta = 10$.
These principles allow constructing the algorithm following Levenberg-Marquardt's approach:

1. Initialisation of λ and (a_0, b_0, R_0) to compute $\mathcal{F}_0 = \mathcal{F}(a_0, b_0, R_0)$.
2. Compute (u_i, v_i, r_i) for all data points (a_k, b_k, R_k).
3. Construct $\boldsymbol{J}^T\boldsymbol{g}$ and $\boldsymbol{N}$.
4. Calculate $\boldsymbol{N}_\lambda = \boldsymbol{N} + \lambda\boldsymbol{I}$, where $\boldsymbol{I}$ is the unitary matrix with dimensions of $\boldsymbol{N}$.
5. Use Cholesky factorisation to solve $\boldsymbol{N}_\lambda\boldsymbol{h} = \boldsymbol{J}^T\boldsymbol{g}$ for $\boldsymbol{h}$.
6. Exit loop if condition $\|\boldsymbol{h}\|/R_k < \epsilon$ is met.
7. Update $a_{k+1} = a_k + h_1$, $b_{k+1} = b_k + h_2$, $c_{k+1} = c_k + h_3$, where (h_1, h_2, h_3) are the components of $\boldsymbol{h}$.
8. Calculate $\mathcal{F}_{k+1} = \mathcal{F}(a_{k+1}, b_{k+1}, R_{k+1})$.
9. If $R_{k+1} \leq 0$ or $\mathcal{F}_{k+1} \geq \mathcal{F}_k$ set $\lambda \to \beta\lambda$ and go to step 4.
   Else increase k by one, set $\lambda \to \alpha\lambda$ and go to step 2.

The values (a_0, b_0, R_0) are initialised by a flat random distribution in the interval $[-30, 30]$ mm for a_0 and b_0. $R_0 \in [70, 120]$ mm is chosen, corresponding to the size and position of the Elementary Cells in x-direction. These values are distributed with a large margin around the estimated true values, which are expected at $(0, 0)$mm to assert the minimisation to convert to the global minimum instead of favouring local minima, which could be the case when choosing fixed initial values (a_0, b_0, R_0). The random number generator of the GEANT4 toolkit is used for this initial guess.
The approach of using a random initial guess drastically decreases the peril of favouring a local minimum in the majority of fits. However, at the same time, it allows the fit to diverge in a significant number of situations. The divergence is subject to *escape valleys*, which exist in virtually every typical data set as shown in section 3.7 of [60]. These are not local minima but decrease strictly monotonic for one of the parameters when minimising $\mathcal{F}$. If the random initial guess is set on the decreasing slope of such a valley, the fit will diverge to infinity.

C Bibliography

[1] Lyndon Evans and Philip Bryant. Lhc machine. *Journal of Instrumentation*, 3(08):S08001, 2008.

[2] CERN document server CERN. The cern accelerator complex, complexe des accélérateurs du cern. https://cds.cern.ch/, 07 2016. accessed 02-June-2017.

[3] CERN. Lhc report: end of 2016 proton-proton operation. https://home.cern/cern-people/updates/2016/10/lhc-report-end-2016-proton-proton-operation, Oct 2016. accessed 08-June-2017.

[4] LHCb Collaboration, AA Alves Jr, et al. The lhcb detector at the lhc. *JINST 3*, S08005:1748–0221, 2008.

[5] LHCb Collaboration. $b\bar{b}$ production angle plots. https://lhcb.web.cern.ch/lhcb/speakersbureau/html/bb_ProductionAngles.html. accessed 06-June-2017.

[6] S. Amato et al. LHCb magnet: Technical design report. Technical report, 2000.

[7] LHCb Collaboration. Tdr: Vertex locator. technical design report. Technical report.

[8] Roel Aaij, A Affolder, K Akiba, M Alexander, S Ali, RB Appleby, M Artuso, A Bates, A Bay, O Behrendt, et al. Performance of the lhcb vertex locator. *Journal of Instrumentation*, 9(09):P09007, 2014.

[9] LHCb Collaboration. Lhcb reoptimized detector design and performance. Technical report, LHCb-TDR-009, 2003.

[10] LHCb Collaboration. Silicon tracker uzh group, material for publications,. http://lhcb.physik.uzh.ch/ST/public/material/index.php, 2014.

[11] R Arink et al. Performance of the lhcb outer tracker, jinst 9 (2014) p01002. *arXiv preprint arXiv:1311.3893*.

[12] LHCb Collaboration. Lhcb inner tracker: Technical design report. *CERN LHCC*, 29, 2002.

[13] LHCb Collaboration. Lhcb outer tracker. technical design report. *CERN LHCC*, 24, 2001.

[14] M Adinolfi et al. Performance of the lhcb rich detector at the lhc. *Eur. Phys. J.*, C73, 2013.

[15] LHCb Collaboration. Lhcb calorimeters technical design report. *CERN/LHCC*, 36:2000, 2000.

[16] LHCb Collaboration. Lhcb muon system: technical design report. LHCC-2001-010. LHCb-TDR-004, 2001.

[17] LHCb Collaboration. Lhcb muon system: Addendum to the muon system technical design report. *CERN/LHCC*, 2:2003, 2003.

[18] A Augusto Alves Jr, L Anderlini, M Anelli, R Antunes Nobrega, G Auriemma, W Baldini, G Bencivenni, R Berutti, A Bizzeti, V Bocci, et al. Performance of the lhcb muon system. *Journal of Instrumentation*, 8(02):P02022, 2013.

[19] R Aaij, J Albrecht, F Alessio, S Amato, E Aslanides, et al. The lhcb trigger and its performance in 2011, 2013.

[20] R Antunes Nobrega, A Franca Barbosa, I Bediaga, G Cernicchiaro, E Correade Oliveira, J Magnin, J Marquesde Miranda, A Massafferri, E Polycarpo, A Reis, et al. Lhcb trigger system: Technical design report. 2003.

[21] Vladimir V Gligorov and LHCb Collaboration. Performance and upgrade plans of the lhcb trigger system. *Nuclear Instruments and Methods in Physics Research Section A: Accelerators, Spectrometers, Detectors and Associated Equipment*, 718:26–29, 2013.

[22] LHCb Collaboration. Letter of intent for the lhcb upgrade. Technical report, CERN-LHCC-2011-001, 2011.

[23] LHCb Collaboration. Framework tdr for the lhcb upgrade: Technical design report. Technical report, LHCb-TDR-012, 2012.

[24] LHCb Collaboration. Lhcb trigger and online upgrade technical design report. Technical report, CERN-LHCC-2014-016, 2014.

[25] LHCb Collaboration. Lhcb pid upgrade technical design report. Technical report, 2013.

[26] LHCb collaboration. Lhcb tracker upgrade technical design report. Technical report, CERN-LHCC-2014-001, LHCB-TDR-015.

[27] Karol Hennessy. Lhcb velo upgrade. *Nuclear Instruments and Methods in Physics Research Section A: Accelerators, Spectrometers, Detectors and Associated Equipment*, 845:97–100, 2017.

[28] Christian Joram, Ulrich Uwer, Thomas Kirn, Blake Dean Leverington, Sebastian Bachmann, Robert Jan Ekelhof, and Janine Müller. Lhcb scintillating fibre tracker engineering design review report: Fibres, mats and modules. Technical report, 2015.

[29] Pavel A Cherenkov. Visible emission of clean liquids by action of γ radiation. *Doklady Akademii Nauk SSSR*, 2:451, 1934.

[30] PA Cherenkov. Influence of magnetic field on the observed luminescence of fluids induced by gamma rays. In *Dokl. Akad, Nauk*, volume 3, pages 413–416, 1936.

[31] I Frank and Ig Tamm. Coherent visible radiation of fast electrons passing through matter. In *Selected Papers*, pages 29–35. Springer, 1991.

[32] Jacques Séguinot and Thomas Ypsilantis. Photo-ionization and cherenkov ring imaging. *Nuclear Instruments and Methods*, 142(3):377–391, 1977.

[33] LHCb Collaboration. Measurement of b-hadron branching fractions for two-body decays into charmless charged hadrons. *Journal of High Energy Physics*, 2012(10):37, 2012.

[34] M Adinolfi et al. Performance of the lhcb rich detector at the lhc. *The European Physical Journal C*, 73(5):2431, 2013.

[35] Thierry Gys. The pixel hybrid photon detectors for the lhcb-rich project. *Nuclear Instruments and Methods in Physics Research Section A: Accelerators, Spectrometers, Detectors and Associated Equipment*, 465(1):240–246, 2001.

[36] C D'Ambrosio and H Leutz. Hybrid photon detectors. *Nuclear Instruments and Methods in Physics Research Section A: Accelerators, Spectrometers, Detectors and Associated Equipment*, 501(2):463–498, 2003.

[37] Stephan Eisenhardt. Production and tests of hybrid photon detectors for the lhcb rich detectors. *Nuclear Instruments and Methods in Physics Research Section A: Accelerators, Spectrometers, Detectors and Associated Equipment*, 595(1):142–145, 2008.

[38] Matthias Moritz, G Aglieri Rinella, Lisa Allebone, Michael Campbell, Thierry Gys, Charlotte Newby, Andrew Pickford, Didier Piedigrossi, and Ken Wyllie. Performance study of new pixel hybrid photon detector prototypes for the lhcb rich counters. *IEEE Transactions on Nuclear Science*, 51(3):1060–1066, 2004.

[39] R Cardinale. The upgraded lhcb rich detector: Status and perspectives. *Nuclear Instruments and Methods in Physics Research Section A: Accelerators, Spectrometers, Detectors and Associated Equipment*, 824:9–11, 2016.

[40] C D'Ambrosio, LHCb RICH Collaboration, et al. The future of rich detectors through the light of the lhcb rich. *Nuclear Instruments and Methods in Physics Research Section A: Accelerators, Spectrometers, Detectors and Associated Equipment*, 2017.

[41] Sajan Easo, LHCb-RICH collaboration, et al. Overview of lhcb-rich upgrade. *Nuclear Instruments and Methods in Physics Research Section A: Accelerators, Spectrometers, Detectors and Associated Equipment*, 2017.

[42] M. K. Baszczyk et al. Test of the photon detection system for the lhcb rich upgrade in a charged particle beam.

[43] L Cadamuro, M Calvi, L Cassina, A Giachero, C Gotti, B Khanji, M Maino, C Matteuzzi, and G Pessina. Characterization of the hamamatsu r11265-103-m64 multi-anode photomultiplier tube. *Journal of Instrumentation*, 9(06):P06021, 2014.

[44] S Gambetta, LHCb RICH Collaboration, et al. First results from quality assurance testing of mapmts for the lhcb rich upgrade. *Nuclear Instruments and Methods in Physics Research Section A: Accelerators, Spectrometers, Detectors and Associated Equipment*, 2017.

[45] Paolo Carniti, Marcello De Matteis, Andrea Giachero, Claudio Gotti, Matteo Maino, and Gianluigi Pessina. Claro-cmos, a very low power asic for fast photon counting with pixellated photodetectors. *Journal of Instrumentation*, 7(11):P11026, 2012.

[46] Hamamatsu. Photomultiplier tubes and photomultiplier tube assemblies r11265u series / h11934 series. https://www.hamamatsu.com/resources/pdf/etd/R11265U_H11934_TPMH1336E.pdf, Feb 2016.

[47] Marta Calvi, Paolo Carniti, Lorenzo Cassina, Claudio Gotti, Matteo Maino, Clara Matteuzzi, and Gianluigi Pessina. Characterization of the hamamatsu h12700a-03 and r12699-03 multi-anode photomultiplier tubes. *Journal of Instrumentation*, 10(09):P09021, 2015.

[48] LHCb RICH Collaboration. Lhcb rich upgrade - production readiness review report for the elementary cell of the photo-detector.

[49] M Andreotti, W Baldini, M Baszczyk, R Calabrese, A Candelori, P Carniti, L Cassina, A Cotta Ramusino, P Dorosz, M Fiorini, et al. Characterization of the 8-channel single-photon counting front-end chip for the upgrade of the lhcb rich detectors. In *Nuclear Science Symposium and Medical Imaging Conference (NSS/MIC), 2015 IEEE*, pages 1–3. IEEE, 2015.

[50] MP Blago and F Keizer. High rate tests of the photon detection system for the lhcb rich upgrade. *Nuclear Instruments and Methods in Physics Research Section A: Accelerators, Spectrometers, Detectors and Associated Equipment*, 2017.

[51] Hamamatsu Photonics K.K. Plp-10 laser diode head series cat. no. socs0003e1. http://www.hamamatsu.com/resources/pdf/sys/SOCS0003E_PLP-10.pdf, Apr 2017.

[52] Hamamatsu Photonics K. K. *Photomultiplier Tubes - Basics and Applications*. 2007.

[53] Linear Technology. Design simulation and device models: Ltspice. http://www.linear.com/designtools/software/#LTspice, 06 2017.

[54] Floris Keizer on behalf of the LHCb RICH Collaboration. (preliminary) comparison between mapmt dynode powering schemes using lhcb rich autumn 2016 testbeam data. Dec 2016.

[55] D Wright et al. Geant4 physics reference manual, 2007.

[56] Inc. Edmund Optics. https://www.edmundoptics.com/optics/optical-lenses/plano-convex-pcx-spherical-singlet-lenses/150mm-dia-x-300mm-focal-length-pcx-condenser-lens/.

[57] M Clemencic, G Corti, S Easo, CR Jones, S Miglioranzi, M Pappagallo, P Robbe, LHCb Collaboration, et al. The lhcb simulation application, gauss: design, evolution and experience. In *Journal of Physics: Conference Series*, volume 331, page 032023. IOP Publishing, 2011.

[58] GAUDI& Barrand, I Belyaev, P Binko, M Cattaneo, R Chytracek, G Corti, M Frank, G Gracia, J Harvey, Eric Van Herwijnen, et al. Gaudi—a software architecture and framework for building hep data processing applications. *Computer Physics Communications*, 140(1-2):45–55, 2001.

[59] Gabriel Taubin. Estimation of planar curves, surfaces, and nonplanar space curves defined by implicit equations with applications to edge and range image segmentation. *IEEE Transactions on Pattern Analysis and Machine Intelligence*, 13(11):1115–1138, 1991.

[60] N. Chernov. Circular and linear regression: Fitting circles and lines by least squares. *Monographs on Statistics and Applied Probability*, 117:256 pp., June 2010.

[61] Nikolai Chernov and Hui Ma. Least squares fitting of quadratic curves and surfaces. *Computer Vision*, pages 285–302, 2011.

[62] Donald W. Marquardt. An algorithm for least-squares estimation of nonlinear parameters. *Journal of the Society for Industrial and Applied Mathematics*, 11(2):431–441, 1963.

[63] R W Forty and O Schneider. RICH pattern recognition. Technical Report LHCb-98-040, CERN, Geneva, Apr 1998.

[64] Vladimir Ivanchenko, Alexei Bogdanov, Alexander Bagulya, Toshiyuki Toshito, Peter Gumplinger, Rostislav Kokoulin, Jean Jacquemier, Vladimir Grichine, Michel Maire, Laszlo Urban, et al. Recent progress of geant4 electromagnetic physics and readiness for the lhc start. *PoS*, page 108, 2008.

[65] Katsuya Amako, Susanna Guatelli, Vladimir N Ivanchenko, Michel Maire, Barbara Mascialino, Koichi Murakami, Petteri Nieminen, Luciano Pandola, Sandra Parlati, Maria Grazia Pia, et al. Comparison of geant4 electromagnetic physics models against the nist reference data. *IEEE Transactions on Nuclear Science*, 52(4):910–918, 2005.

Acknowledgments

I would like to express my gratitude to Prof. Ulrich Uwer for the possibility to write my thesis in his research group, and for providing professional advice and helpful suggestions.
I also offer my special thanks to Priv.-Doz. Dr Kai Schweda for investing his time and patience as a second referee.

I would like to express my very great appreciation to Dr Carmelo D'Ambrosio, for his dedicated and constructive supervision, but above all for his experienced guidance. My grateful thanks are also extended to Dr Sajan Easo for offering help whenever needed and for his enthusiastic encouragement.

I wish to thank the RICH collaboration for providing a very productive and friendly work environment. In particular Silvia and Roberta for their endless patience. Floris, without whom the results presented in this document would not have been the same. Simon and Giovanni for many fruitful conversations. Didier, Thierry, and Christoph for providing technical advice.

I wholeheartedly thank my parents and my brother for their unwavering support.

Erklärung

Ich versichere, dass ich diese Arbeit selbstständig verfasst und keine anderen als die angegebenen Quellen und Hilfsmittel benutzt habe.

Heidelberg, den 21. Juli 2017

_____

Michele Piero Blago